CFD Study of an Over-Wing Nacelle Configuration

Steven H. Berguin,[1] Sudharshan Ashwin Renganathan,[2] Jai Ahuja,[3]
Mengzhen Chen,[3] Christian Perron,[3] Jimmy Tai,[1] and Dimitri N. Mavris[4]
Georgia Institute of Technology, Atlanta, GA, 30332, USA

October 5, 2018

[1]Research Engineer II, School of Aerospace Engineering.
[2]Post-Doctoral Fellow, School of Aerospace Engineering.
[3]PhD Candidate, School of Aerospace Engineering.
[4]Professor, School of Aerospace Engineering.

Executive Summary

Engine bypass ratio (BPR) has grown significantly over the years, due to a desire for increased efficiency, and the large fan diameters that have resulted are forcing the engines so close to the wing that there is no room left for them to grow any larger due to ground clearance constraints. As BPR increases even further in the future, conventional Under-Wing Nacelle (UWN) installations will therefore no longer be possible without drastic modification of the wing and landing gear. Over-Wing nacelle concepts solve this problem by offering a convenient installation for high BPR turbofans and, additionally, offer the potential to mitigate community noise through engine noise shielding using the wing as a shield. However, OWN has historically warranted concern about unacceptably high drag levels at transonic speeds and the purpose of this research was to determine whether or not drag can be improved enough to take advantage of the aforementioned cross-disciplinary benefits. To do so, three studies were conducted: study 1 conducted a simple nacelle sweep in order to identify and visualize the physical mechanisms driving the configuration, study 2 then conducted a sensitivity analysis in order to understand important design variables and, finally, study 3 performed single point optimization for a trailing edge OWN concept. Overall, results suggests that OWN drag can be improved to levels commensurate with its Under-Wing Nacelle (UWN) counterpart. However, limitations of the analysis tools employed for this research (in the area of shape optimization) were insufficient to outperform the UWN baseline. Such limitations were successfully overcome by modern OWN concepts, such as the Honda Business Jet and the military Lockheed HWB for air mobility missions. Overall, it is therefore the authors' opinion that either leading-edge or trailing-edge mounted OWN configurations are concepts worth investigating further for civil transport applications, using state-of-the-art multidisciplinary analysis and optimization tools for engine-airframe integration.

Contents

Chapter 1

Introduction

1.1 Research Objectives

Historically, for the vast majority of commercial transports, engines have been mounted under and ahead of the wing for large airplanes. Experience has shown that such conventional locations are effective choices for reducing installation drag to acceptably low levels [1], and industry has not had reason to venture outside this envelope of low-risk engine installations. However, due to a desire for increased efficiency, engine bypass ratio (BPR) has grown significantly over the years, and the large fan diameters that have resulted are forcing the engines so close to the wing that there is no room left for them to grow any larger due to ground clearance constraints. As BPR increases even further in the future, conventional Under-Wing Nacelle (UWN) installations will therefore no longer be possible without drastic modification of the wing and landing gear.

Alternatively, engines could be placed above the wing in an Over-Wing Nacelle (OWN) configuration; a convenient installation for high BPR turbofans, which additionally offers the potential to mitigate community noise. As explained by Berton [2], modern high BPR engines extract significantly higher amounts of energy from the core flow, effectively reducing the velocity differential between the core jet and fan discharge during takeoff. This significantly reduces downstream jet noise, leaving upstream fan noise as a dominant source that can be effectively shielded by the wing. Other advantages of OWN include: shorter and more robust landing gear, reduced Foreign Object Damage (FOD) risk, and possible Shorter Take-Off and Landing (STOL) due to powered lift. OWN has historically warranted concern about unacceptably high drag levels at transonic speeds; however this preconception has been disproven in recent studies [3, 4, 5], resulting in renewed interest for this concept.

This work seeks to offer an independent assessment that corroborates the aforementioned, more recent studies. This is accomplished by exploring the design space of a notional 300-passenger class civil transport with high-bypass turbofans of the 94,000 lb thrust class, mounted over the wing, for a continuum of flight conditions ranging from Mach 0.7 to 0.9 at fixed C_L. The two responses under consideration are installation drag ΔC_D and relative change in pressure recovery ΔPR as a function of three design variables, selected based on the outcome of a screening test: nacelle chord-wise location X, height above the wing Z, and cruise Mach number M. The Outer Mold Line (OML) is optimized using free-form deformation and adjoint methods for each design combination. All data is generated using the Reynolds Averaged Navier-Stokes (RANS) equations with a validated CFD model of the NASA Common Research Model [6] (CRM), modified with over-wing engines. This report is organized into 6 chapters. The remainder of this chapter describes the research plan, chapter 2 provides general background on OWN concepts, chapter 3 details the modeling and simulation environment, chapter 4 conducts a simple nacelle sweep to obtain preliminary trends, chapter 5 summarizes the results of a sensitivity analysis, chapter 6 explores the design space and, finally, chapter 7 draws conclusions.

1.2 Scope

The field of Propulsion-Airframe Integration (PAI) can be described as a multi-disciplinary optimization problem involving aerodynamics, propulsion, and structures. Depending on the engine installation, the presence of the engine near wing will distort the aerodynamic flow-field and, in return, aerodynamic phenomena such as shock waves or boundary layer separation may deteriorate engine performance. Furthermore, the forces exerted by the engine impart deformations on the wing, which must be accounted for in the aerodynamic solution. While such inter-disciplinary coupling is well-understood for conventional, under-wing installations, it is not the case for unconventional installations such as over-wing nacelles.

Moreover, beyond multi-disciplinary considerations, the engine installation must account for different operating conditions. On one hand, off-design constraints such as takeoff and Extended Twin-Jet Operations, which imposes additional engine inoperative design requirements for cruising with one engine out at high speeds, must be considered within the design problem. On the other hand, multiple on-design conditions must be taken into account in order to ensure realistic airfoil designs (*i.e.* robust shapes that work well over a range of flight conditions encountered at cruise).

However, the complexity of accounting for the multi-disciplinary and multi-point aspects of this problem is not worth the effort, unless it can first be shown that an over-wing nacelle design is capable of out-performing a baseline, under-wing design under ideal conditions. As a consequence, this research only addresses a single design point, uncoupled aero-propulsion optimization problem for OWN.

1.3 Research Plan

The research plan and general organization of this report is briefly described here-under. Broadly speaking, there were two parts to this research. The first part focused on capability development and background research, while the second focused on analysis.

1.3.1 Literature Review

Good engineering practice suggests that the design of a new airplane configuration should always start where history left off. To do so, a literature was conducted in order to better understand what has already been done with respect to over-wing nacelles. OWN literature was found to be dispersed and rather scarce and, therefore, the result of this review provides a useful synthesis that can be used as a starting point for other researchers. The outcome of this task is summarized in chapter 2.

1.3.2 Modeling and Simulation Framework Development

In order to study OWN concepts, two things are needed: a validated CFD model of the aircraft configuration and a simulation framework to evaluate it. The former involves creating a baseline geometry, generating surface and volume grids, setting up boundary conditions, solving the Reynolds Averaged Navier-Stokes (RANS), and checking the results against some known validation data. To do so, the baseline airframe was taken to be the NASA Common Research Model (CRM) because it is representative of modern civil transports, publicly available, and well studied. However, translating the nacelle above the wing will alter the flow-field in a way that the baseline CRM geometry was not designed for. Hence, in order to capture any benefit OWN may have to offer, an aerodynamic shape optimization framework is needed to re-design the wing airfoil shapes. The outcome of this task is summarized in chapter 3.

1.3.3 Configuration Analysis and Optimization

The objective of this task is to understand what physical phenomena drive OWN performance, identify any cross-disciplinary trade-offs between propulsion and aerodynamics, quantify design trends such a drag rise as a function of nacelle location and, finally, uncover any feasible regions of the design space that would justify pursuing this concept further for civil aviation. Three studies have been devised in order to do so; they are described next. The outcome of this task is summarized in chapters 4–6.

Study 1: Simple Nacelle Sweep

The objective of this study is to quantify preliminary design trends in order to develop intuition about the physics driving OWN concepts. A Through-Flow Nacelle (TFN) is translated horizontally from leading edge to trailing edge at the cruise flight condition, holding the lift coefficient fixed. The OML is not re-optimized. Drag coefficients are plotted as a function nacelle location and the flow-field is examined using CFD visualization tools (Mach and pressure contours). The details of this study is described in chapter 4.

Study 2: Sensitivity Analysis

The objective of this study is to quantify the strength of aero-propulsive coupling for podded OWN. This is accomplished using statistical analysis to quantify the sensitivity of powered effects on installation drag, engine pressure recovery, and lift curve characteristics at cruise as a function of nacelle XYZ location and power setting. The OML is not re-optimized. The details of this study is described in chapter 5.

Study 3: Single-Point Optimization

The purpose of this study is to answer the question: is it possible to re-design the outer mold line such that the aerodynamic performance of OWN be made on par or better than the UWN baseline? This is accomplished by using optimal design methods to shape the Outer Mold Line (OML) and comparing the results to those of the UWN baseline, under rigid body assumptions and ignoring trim drag. The reasoning being that if one cannot achieve comparable aerodynamic performance under restricted assumptions, then there is no reason to pursue a more complicated analysis. While it was originally planned to investigate a large number of OWN engine placements, time constraints only allowed for one case to be run, selected to be an OWN trailing edge location based on findings from the literature review and study 2.

1.4 Project Management and Resources

The team structure is presented in Fig. 1.1. It consisted of four PhD students led by one project manager under the direction of two principal investigators. Students were selected based on their interest in the topic and background in fluid mechanics.

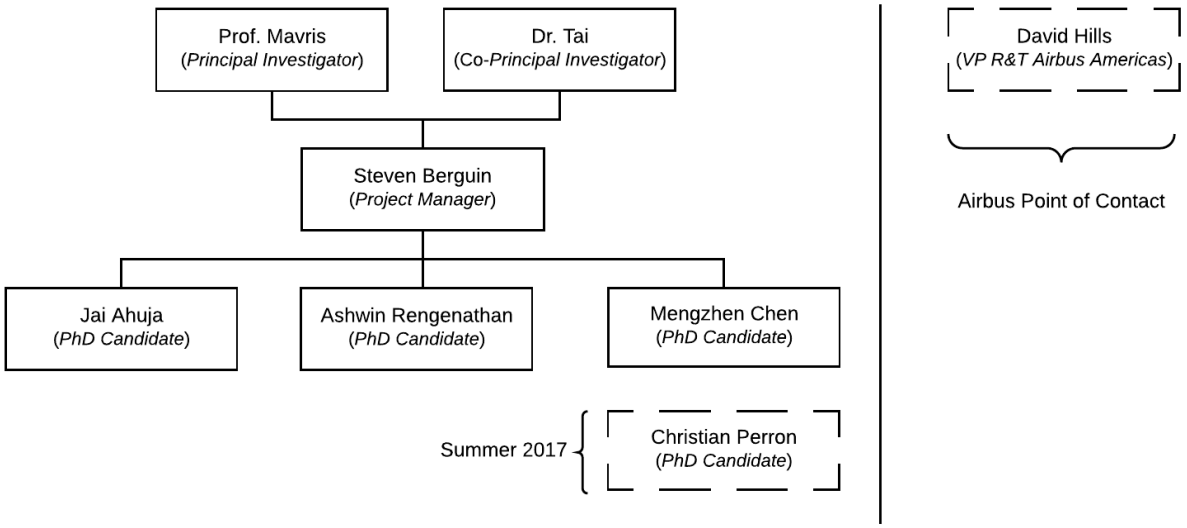

Figure 1.1: Team structure

Given the small size of the project, it was convenient to use Dropbox Enterprise and GitHub Enterprise in order to manage all work products, as shown in Fig. 1.2. Documents, models, and results were stored

on Dropbox, while the modeling and simulation environment was maintained on GitHub[1]. Access will be granted upon request.

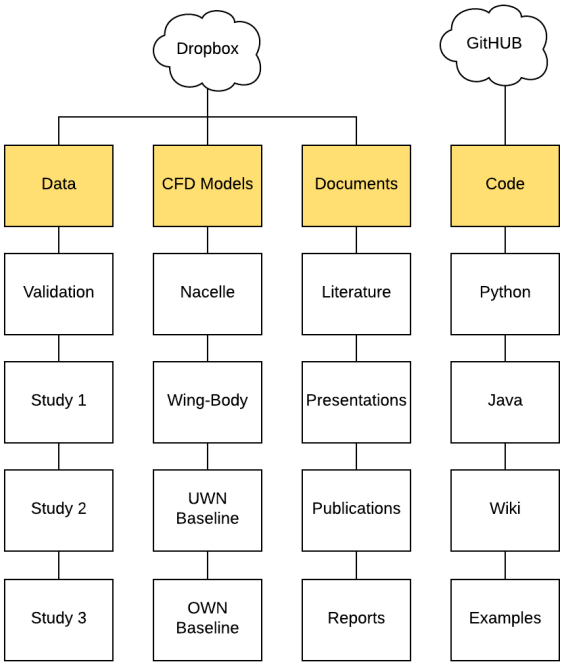

Figure 1.2: Data management

Finally, the team had access to one workstation with 64GB of RAM and two clusters, as shown in Fig. 1.3. The small cluster had 168 CPU's and was used for development (*e.g.* running Euler test cases), while the large cluster had 768 CPU's and was used to generate all results.

[1]https://github.gatech.edu/sberguin3/STAR-ASO.git

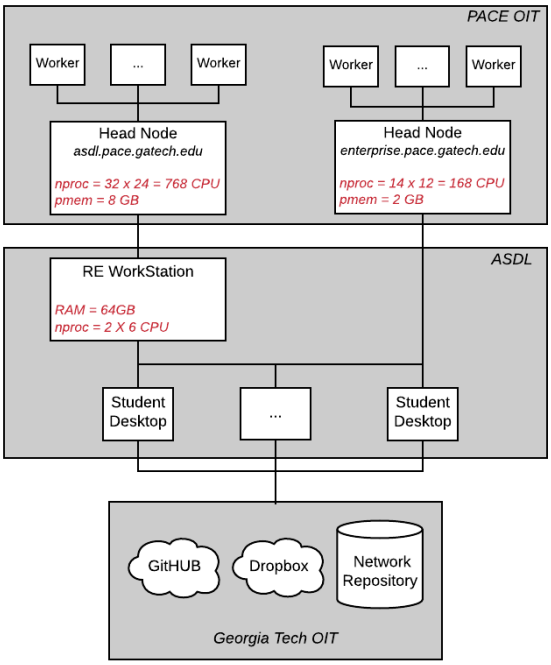

Figure 1.3: Computational resources

Chapter 2

Over-Wing Nacelle Background

Good engineering practice suggests that the design of a new airplane configuration, whether it is evolutionary or revolutionary, should always start where history left off. The purpose of this chapter is therefore to provide a literature review of historical OWN concepts to the best of the authors' knowledge.

2.1 Experimental and Numerical Studies

In 1973, Putnam [7] setup a wind-tunnel model to simulate the effects of the exhaust jet blown over the upper wing surface and found that (i) jet blowing increases the zero-lift drag of the wing and that (ii) the nacelle had to be placed about 1.5 nozzle exit diameters above the wing and $2.5 - 4.5$ nozzle exit diameters upstream of the wing leading edge in order to minimize interference. In 1979, Reubush [8] tested a scaled OWN model in a wind-tunnel and observed that minimum wing-body drag occurred at forward engine placements, when the nacelle exit plane was located one nacelle diameter aft and vertically above the wing leading edge at 50% wing span. However, shapes were fixed and nacelles were non-metric, meaning that any counter-acting penalties incurred on the nacelle could not be measured. The author also found that airframe drag was insensitive to engine power setting. In 1983, Henderson et al. [9] revisited this configuration using a fully metric model this time and found that, indeed, nacelle penalties did outweigh the previously reported benefits for the wing-body; but they also found that interference drag could be reduced significantly just by re-contouring the nacelles. In the same year, Szodruch [10] conducted a fully metric wind-tunnel study with powered nacelles and concluded that "over-the-wing engines yield higher maximum lift-drag ratios than under-the-wing arrangements [but that] optimum nacelle positions are dependent on the wing configurations." Of particular relevance, they also found that both the jet and intake flows are important for interference effects.

All aforementioned studies focused on forward-mounted engines, where the nacelle is either ahead or in the vicinity of the wing leading edge. However, modern OWN studies tend to favor trailing edge installations. For instance, in 2003, Fujino et al [3] found that aft-nacelle locations lead to optimal wave drag levels, below that of the clean wing in their case. More recent CFD studies by Hooker et al. [4, 5] in 2013 and 2014 were comprehensive in finding that optimal OWN installation locations combined with wing shape optimization can lead to 5% improvement in aerodynamic efficiency, reduce wing weight and improve community noise levels compared to a representative UWN baseline.

2.2 Historical Concepts

The previous section marks a quest for energy efficiency at transonic speeds. However, this design objective is in contrast with historical OWN applications, which sought to design for STOL. In fact, this is most likely the reason why OWN concepts are historical perceived to be "energy inefficient" at high speeds: they weren't designed for it. To that effect, this section briefly summarizes some notable OWN airplanes that once flew.

Figure 2.1: Historical OWN Concepts

2.2.1 Boeing YC-14 (1970's)

Wimpress et al. [11] explain that the Boeing YC-14, shown in Fig. 2.1, was a military experimental aircraft meant to replace the Lockheed C-130 and capable of carrying large, bulky payloads such as tanks or trucks into and out of short unprepared airfields. It was designed at the outcome of the Vietnam conflict, where it had become apparent that the Air Force faced an airlift dilemma. On one hand, airplanes such as the Lockheed C-141 and C-5A had good payload capability, range and speed; however, they required elaborate air bases with long, paved runways to operate effectively. On the other hand, helicopters could operate from anywhere, but they were slow, vulnerable and could only carry cargo over limited range. In order to solve this dilemma, the Air Force set out to acquire a tactical aircraft that could "interface effectively with the heavy logistics transports and carry men and materials to a point where they could be used directly by the operational troops or picked up and delivered efficiently by helicopters" [11]. This required the airplane to takeoff and land out of 2,000 feet unprepared runways, and carry a 38,000 lb payload over 2,600 nm.

The final prototype resulted in a high wing, T-tail configuration with supercritical airfoils and over-wing nacelles featuring revolutionary Upper Surface Blowing (USB) technology that enabled the YC-14 to reach a maximum lift coefficient of 3.3 at 89 knots [12]. The airplane was originally designed to cruise at Mach 0.74, but it was soon discovered that holding such a high cruise speed conflicted with the requirement to have very high lift. The former favored a swept wing, whereas the latter favored a straight wing [11]. In order to satisfy Short Take-Off and Landing (STOL) requirements, the Air Force eventually relaxed the cruise speed to Mach 0.66 [12]. Unfortunately, by the time the YC-14 was ready for production, military priorities had changed and the Air Force decided it needed a larger transport that would fly to standard, conventional

airfields rather than into battle zones.

2.2.2 Fokker VFW-614 (1970's)

The first and only commercial transport ever introduced with an over-wing nacelle concept was the Fokker-VFW 614, a quiet short haul airliner designed to cruise at Mach 0.65, shown in Fig. 2.1. The description by Kathen [13] suggests that the airplane was developed with the vision of capturing a then yet untapped market for small capacity, short haul transport, which is today dominated by airplanes such as the Canadair CRJ or the Embraer ERJ families. It specifically targeted small provisional airfields with low traffic density, and short, potentially unprepared runways. The airplane measured 70.5 ft in span, 67.5 ft in length, and had a maximum takeoff weight of 44,000 lb, capable of accommodating up to 44 passengers. It was designed for low maintenance, high payload configuration flexibility, quick turn around time, and short takeoff and landing [13].

The top-mounted nacelles allowed ground clearance constraints to be relaxed, resulting in shorter robust landing gear, easier payload access and reduced risk of foreign object damage. As a welcome but unintended benefit of the engine location, the shielding effect of the wing made the VFW-614 the most quiet airplane of its time [13]. However, despite its capabilities, the VFW-614 program was canceled in 1977 due to a lack of demand. In the present authors' opinion, it is reasonable to conjecture that this is perhaps because the market for regional jet transport did not pick up until years later. Today, it still flies as a research aircraft known as the Advanced Technology Testing Aircraft System (ATTAS) operated by the Deutschen Zentrums für Luft- und Raumfahrt (DLR). While its example provides evidence for the advantage of noise shielding in commercial applications, it is safe to say that at Mach 0.65 the VFW-614 did not experience transonic wave drag.

2.2.3 ASKA (1970's)

The ASKA shown in Fig. 2.1 was a four-engine research aircraft developed by the Japanese National Aeronautics Laboratory (NAL) to investigate the applications of Upper Suction Blowing (USB) technology on commercial transports [14]. It was a conversion of the Kawasaki C-1 into a USB powered-lift aircraft, capable of Short Take-Off and Landing (STOL) by taking advantage of the Coandă effect. While the airplane performed successfully well at low speeds [14], it was never designed for high-speed flight [15]. It's intended cruise speed was Mach 0.565 [12]. As a consequence, at transonic speeds, it suffered a plethora of aerodynamic inflictions ranging from strong shock waves and boundary layer separation to scrubbing drag and buffeting between the nacelles [14]. In fact, the design culminated into installation drag reaching 80 percent of the wing-body drag [14], an unacceptably high number for any airplane. However, this is not typical of OWN concepts that employ USB technology. During the development of the YC-14 for example, a staple of USB technology, Wimpress et al. [11] recall an exchange with high-speed aerodynamicists at NASA where the authors revealed that "Boeing had solved, very successfully, the high-speed drag problem of over-wing nacelles," before the air-force eventually relaxed the target cruise speed from Mach 0.74 to Mach 0.66 for other reasons. Thus, care must be taken not to make a hasty generalization out of the ASKA experience.

2.2.4 NASA QSRA (1970's)

As explained by Hall [16], the Quiet Short-Haul Research Aircraft (QSRA), shown in Fig. 2.1, was a research aircraft developed to investigate the application of upper surface blowing for quiet short takeoff and landing. Powered lift was generated using four high-bypass turbofan engines blowing the exhaust over the top surface of the wing. By taking advantage of the Coandă effect, the flow could be deflected downwards using a curved trailing edge flap, effectively converting a portion of the thrust into lift. However, an important feature of the QSRA was to achieve this at a low noise level. It successfully accomplished this using the wing to shield the noise produced by the jet exhaust. Combined with the help of additional acoustic materials through the engine, the noise foot print of the QSRA was as small as 1/7 of an equivalent transport of that period [16]. However, "the QSRA was designed solely as a low-speed research aircraft" [16], which means it was not intended for transonic flight. Even though the isolated wing itself was capable of efficient cruise at Mach 0.74, the airplane as a whole was not designed for those speeds [16].

2.3 Synthesis of Literature Review

This brief review of OWN concepts serves to emphasize that the idea of placing the engines over the wing is not new; however, what is different today is the design objective. Historically, the primary application of over-wing nacelles has been short takeoff and landing. This was true for the Boeing YC-14, the ASKA, and the QSRA for example, which all feature Upper Surface Blowing (USB) technology. The only commercial application to date is the VFW-614, but it flew at subsonic speeds. Today, the design driver for OWN is energy efficiency with notable examples being the Honda Business Jet, a small business jet currently in service with a 600 *lb* payload, and the Lockheed HWB, a large military airlifter not yet built with a 220,000 *lb* payload. However, since a civil transport lies somewhere in-between with a 35,274 *lb* max payload for A350-90, it still remains to be determined if OWN benefits translate to commercial aviation.

Chapter 3

Modeling and Simulation

This chapter describes the modeling and simulation environment used to capture the physics and conduct aerodynamic shape optimization. As shown in Fig. 3.1, capability development can be organized into two parallel efforts: modeling and simulation. Modeling consists of developing validated CFD models of the airframe and engine, while simulation consists of stitching codes together to perform aerodynamic shape optimization. This chapter describes the result of both efforts.

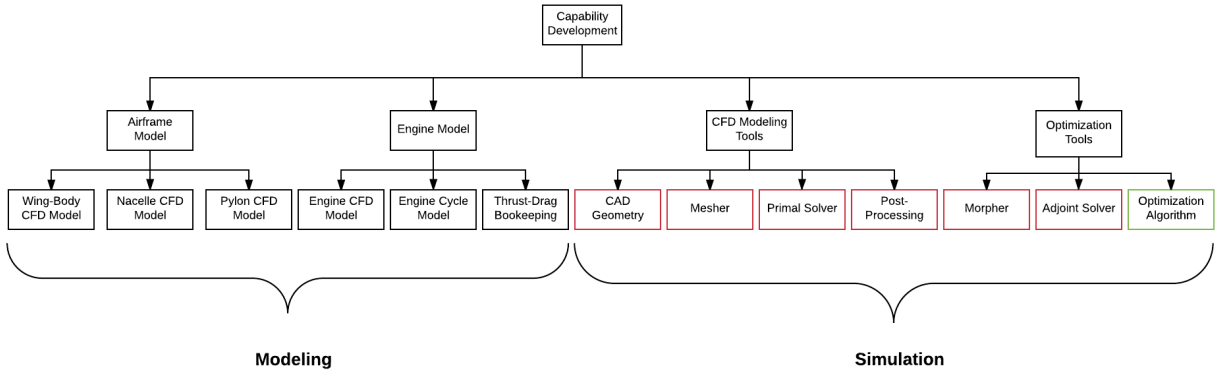

Figure 3.1: Components of the modeling and simulation environment. *Black boxes represent STAR-CCM+ models, red boxes are capabilities available within STAR-CCM+, and the green box is a Python capability.*

3.1 Physics-Based Models

All physics were captured using the commercial CFD software STAR-CCM+. The steady-state Reynolds-Averaged Navier-Stokes (RANS) equations were solved using the commercial software STAR-CCM+ assuming a fully turbulent boundary layer with K-Omega SST (Menter) turbulence model. The solver uses a finite volume approach with implicit time integration scheme and 2nd order upwind spatial discretization. The flux at the boundary is reconstructed using Roe flux difference splitting with the Venkatakrishnan limiter. The Courant number was set to 10 and, to accelerate convergence, an Algebraic Multi-Grid (AMG) method was used with 30 V-cycles and a Gauss-Seidel relaxation scheme.

3.1.1 Airframe Model and Validation

The baseline aircraft is the NASA Common Research Model [6] modified with over-wing nacelles at $C_L = 0.5$, $M = 0.85$, and an altitude of $10,668m$. The pylon and tail are not considered in this study. Known geometry issues [17] with the fuselage fairing and nacelle necessitated minor modifications to repair self-intersecting

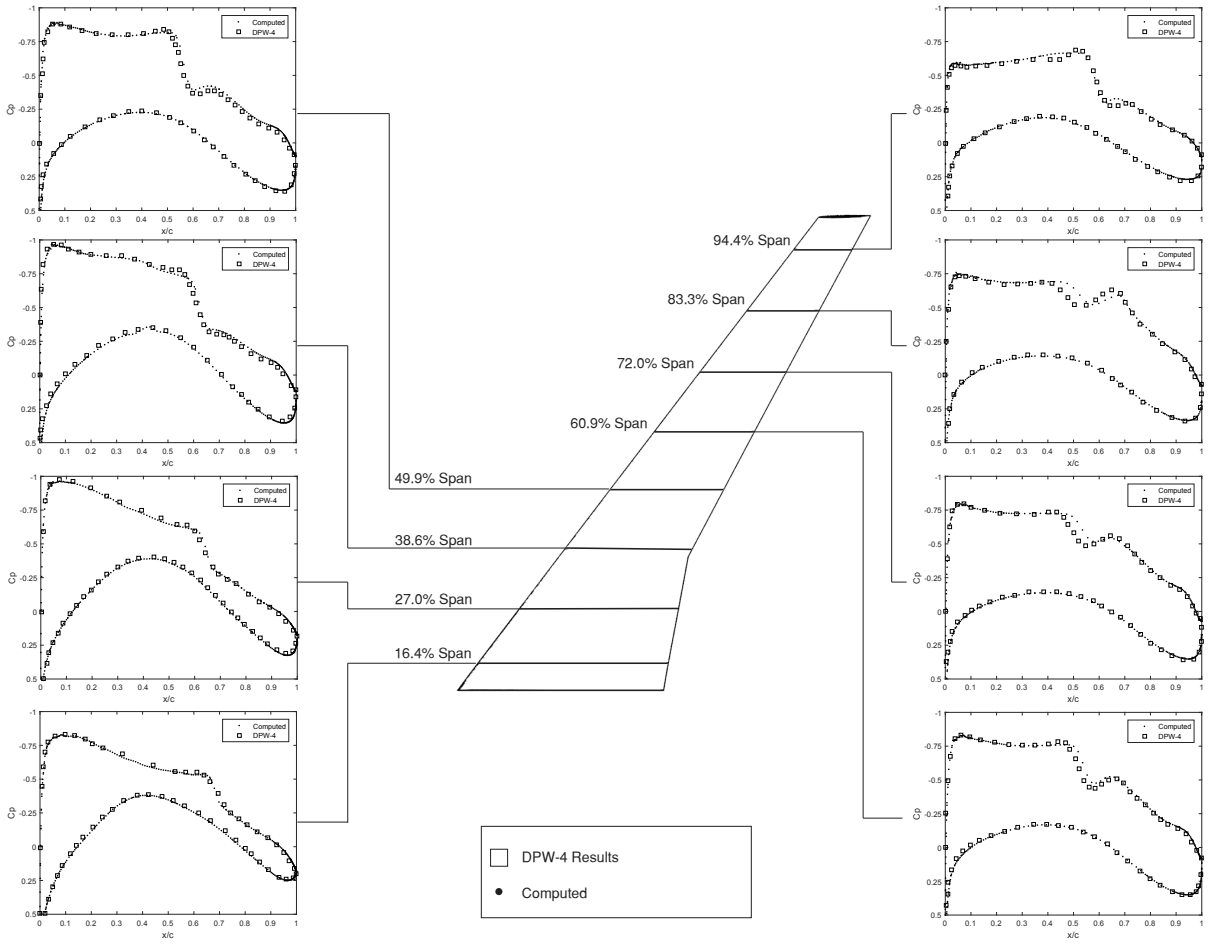

(a) CRM wing-body validation against DPW-4 [6]

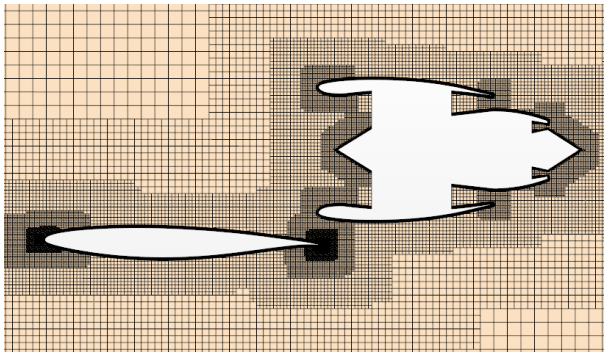

(b) Wing-Body-Nacelle (WBN) mesh – $\mathcal{O}(30M)$ cells

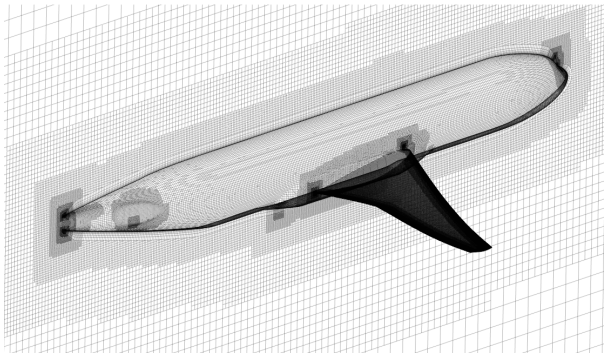

(c) Wing-Body (WB) mesh – $\mathcal{O}(24M)$ cells

Figure 3.2: CRM wing-body at $C_L = 0.5$, $M = 0.85$, $Re = 40M$

surfaces and close gaps; however the wing is unchanged. The study was conducted using an unstructured Cartesian mesh, as shown in Figure 3.2b, augmented with 30 layers of high aspect ratio prism cells near the surface to resolve the boundary layer. Choosing a $y+$ value of 1 resulted in a near wall cell height of $5.34e{-}5$. The final mesh contained $\mathcal{O}(24M)$ cells for the Wing-Body (WB) and $\mathcal{O}(30M)$ cells for the Wing-Body-Nacelle (WBN), resulting in a CPU Time per solver iteration of approximately 4 $cpu \cdot min/iteration$ for the wing-body and 5 $cpu \cdot min/iteration$ for the wing-body-nacelle. Model validation is provided in Figure 3.2a

for the wing-body by comparing the computed pressure coefficient distributions with those obtained by Vassberg [6]. Good agreement is observed between the two sets of data.

3.1.2 Powered Nacelle Model and Validation

The engine was simulated in CFD by imposing flow boundary conditions at the fan-face, bypass nozzle plenum, and core nozzle plenum as shown in Fig. 3.3. Thermodynamics properties at each of these boundary conditions were obtained from a simulated model of a notional high bypass turbofan of the 94,000 lbs thrust class turbofans sized for a representative twin-aisle mission with a cruise design point of $C_L = 0.5$, $M = 0.85$, and altitude of $10,668\ m$. This engine was selected because it was readily available and the CRM does not have an "official" engine cycle publicly available; only a through-flow nacelle. The engine model was developed (and calibrated) using publicly available information, following a rigorous multi-design point vehicle sizing process known as the Environmental Design Space (EDS) [18]. However, there is a limitation: the CRM nacelle inlet is oversized for this engine. As a consequence, spillage was higher than what is typically expected at cruise but deemed acceptable since the study is only considering relative changes.

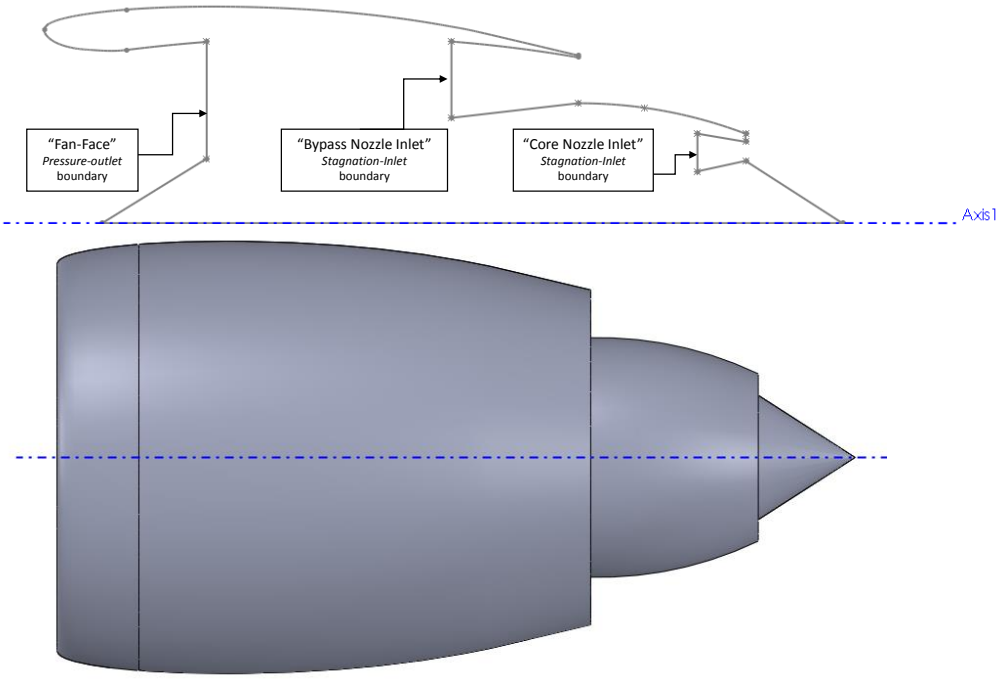

Figure 3.3: Powered nacelle geometry and boundary conditions

Table 3.1: Verification of RANS prediction of engine thrust

	EDS	CFD	Error(%)
Inlet massflow rate (lb/s)	1345.88	1502.79	10.44
Bypass nozzle massflow rate (lb/s)	1195.52	1143.352	-4.56
Core nozzle massflow rate (lb/s)	143.57	151.0188	4.93
Engine net thrust (lbf)	19,600	18,820	-4.14

The nominal CRM nacelle is asymmetric but, for convenience, it was modified to be symmetric such that the entire engine geometry, including the core, could be obtained by revolving the profile section shown in Fig. 3.3. The boundary conditions used to simulate the powered nacelle were a pressure-outlet condition at the fan-face and stagnation inlet conditions at the bypass and core nozzle plenums. As a verification, the isolated engine was simulated in CFD at cruise conditions of $M = 0.85$ and altitude of $10,668\ m$ with zero

incidence angle and compared against EDS in in Table 3.1. Net thrust agreed within 10% which was deemed acceptable since a discrepancy between 3D RANS predictions and 1D cycle analysis is expected.

3.2 Simulation Framework

As shown in Fig. 3.1, STAR-CCM+ provides all the elements blocks necessary to conduct aerodynamic shape optimization (*i.e.* primal solver, adjoint solver, free-form deformation), except the optimization logic. In order to overcome this shortcoming, an Aerodynamic Shape Optimization (ASO) framework was developed as shown in Fig. 3.4. The source code, documentation, and explanatory examples are available on GitHub[1] for the interested reader. The purpose of this section is to provide validation results in order to check that the optimization framework is working properly.

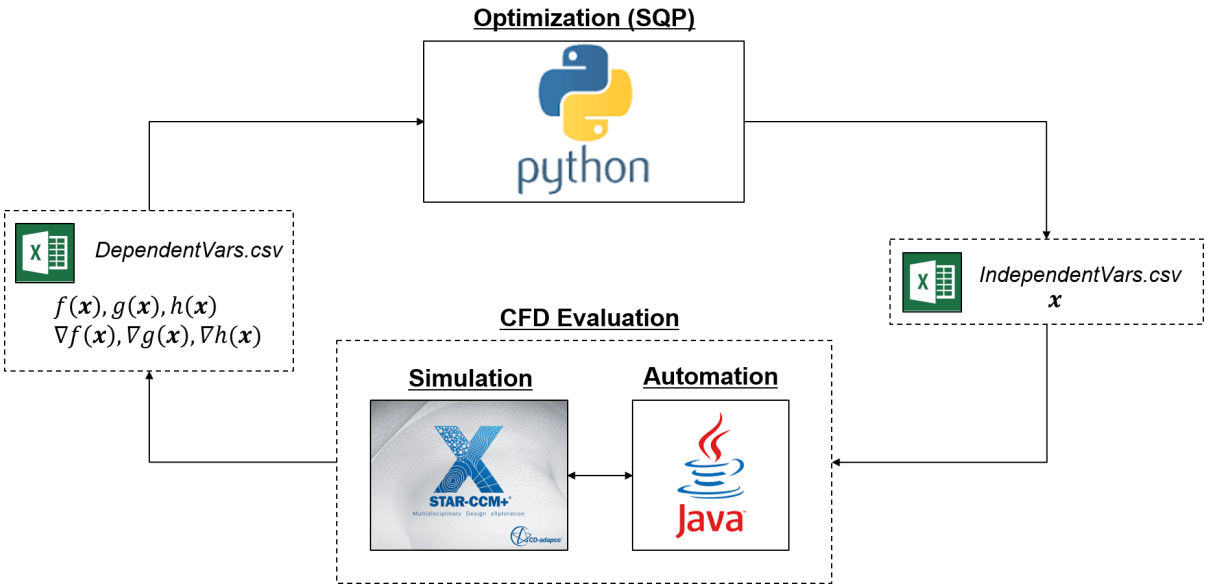

Figure 3.4: Optimization Framework. *Optimization is conducted in python, which updates the design variables (control point z-coordinates) by writing them to a CSV file that is then read into the CFD environment using class packages written in the STAR-CCM+ Java API. CFD automation then consists of morphing the geometry based on the new control point locations, running the primal solution, and computing the gradient using adjoint methods. Pertinent outputs such as gradients, constraints, and objective function are finally written to a CSV file in a format that can be read back into Python. The process is repeated until convergence.*

3.2.1 Validation: Inviscid RAE 2822 Optimization

In a first step, it was decided to check the setup using a simple 2D test case, taken to be the TE3 test case from the European Computational Aerodynamics Research Project (ECARP) [19]. The problem consists of optimizing the RAE 2822 airfoil at $M_\infty = 0.73$ and $\alpha = 2$ degrees, subject to a fixed lift constraint and constant angle of attack. The parameterization used for this work is shown in Fig. 3.5a, while results are compared to those presented by Bock and Haase [19] in Figs. 3.5c–3.5d and Table 3.2.

Overall, good agreement was observed . The optimized airfoil shapes are reasonable close to those obtain by the other authors and, similarly, the pressure coefficient distributions match within reason, indicating that the framework is setup correctly. Discrepancies are most likely attributable to differences in the CFD solvers, optimizer algorithms, and airfoil shape parameterization.

Finally, it is acknowledge that C_D does not go to zero, even theory predicts that it should in the absence of wave drag. While this was initially concerning, it was eventually observed that repeating the same

[1] https://github.gatech.edu/sberguin3/STAR-ASO.git

optimization process on progressively finer and finer grids drives the drag coefficient closer and closer to zero. This discrepancy was thus attributed to numerical error in the solver due to domain discretization and not investigated further.

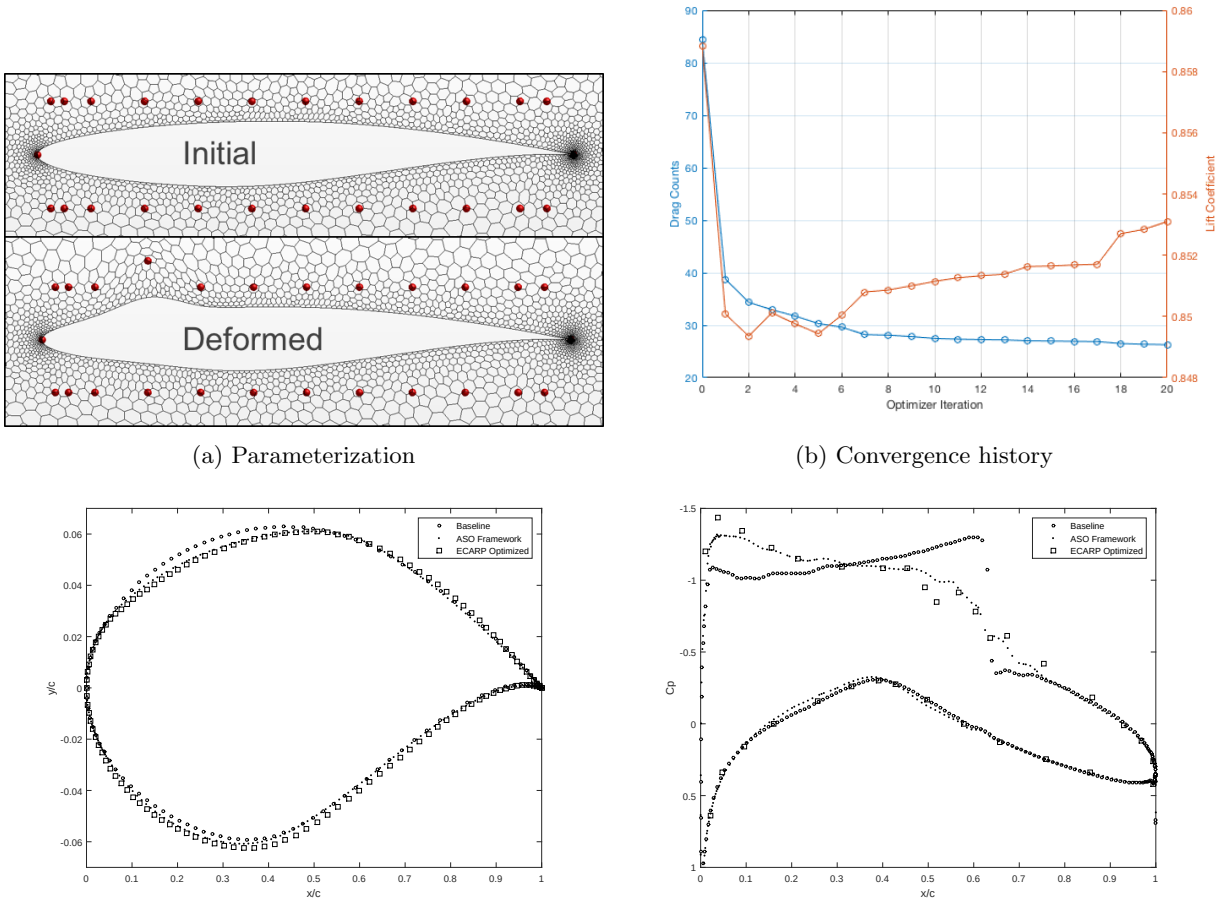

(a) Parameterization

(b) Convergence history

(c) Airfoil Shapes

(d) Pressure Coefficient

Figure 3.5: RAE 2822 validation against ECARP [19]

Table 3.2: Comparison of computed RAE 2822 C_D and C_L values with those from ECARP

	C_D	C_L
ECARP Baseline	0.006653	0.869
ASO Framework Baseline	0.007852	0.860
ECARP Optimized	0.000024	0.869
ASO Framework Optimized	0.001816	0.848

3.2.2 Validation: Inviscid Onera M6 Optimization

A natural progression from the airfoil validation case is the Onera M6 wing. An inviscid lift and moment constrained drag minimization of the Onera M6 at $M_\infty = 0.84$ and $\alpha = 3.06$ degrees is conducted, and the results are compared to those obtained by Selmin for the ECARP test case TE6 [19]. Fig. 3.6 shows the optimizer convergence history for aerodynamic coefficients. The dashed lines indicate target values for

the lift and moment equality constraints. Fig. 3.7 compares the baseline and optimized pressure coefficient distribution on the upper surface of the wing. Table 3.3 compares the values aerodynamic coefficients.

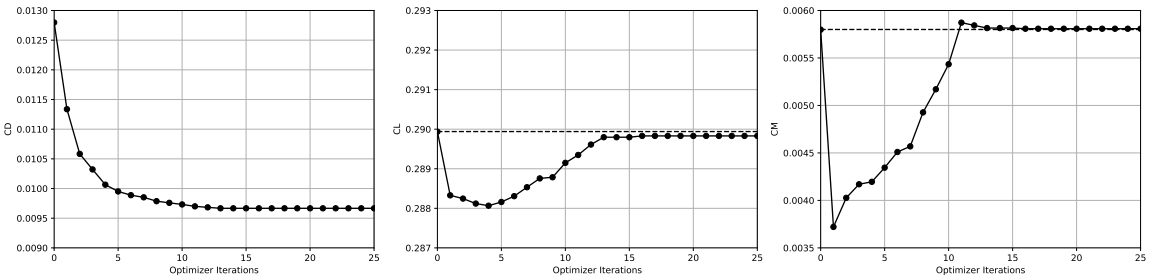

(a) C_D (b) C_L (c) C_M

Figure 3.6: Optimizer convergence history

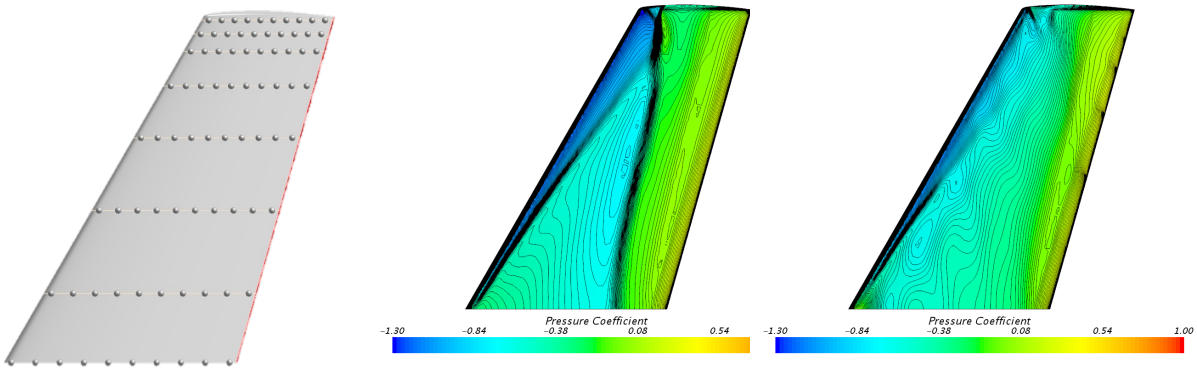

(a) Parameterization (b) ASO Framework Baseline (c) ASO Framework Optimized

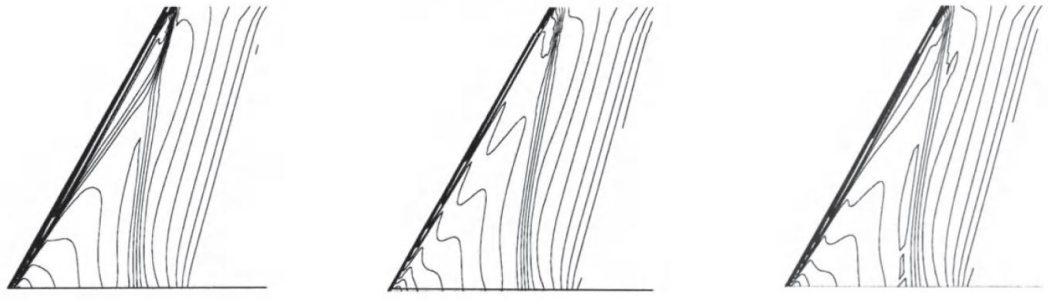

(d) ECARP Baseline (e) ECARP Optimized Case 1 (f) ECARP Optimized Case 2

Figure 3.7: ONERA M6 validation against ECARP [19]

Differences between the ECARP and the ASO Framework results are most likely due to the parameterization of the geometry. Selmin performs two optimization cases, first modifying the root section and scaling the changes along the span, and second modifying both the root and tip sections simultaneously. For the ASO Framework validation case, 8 airfoil sections are defined along the span as seen in Fig. 3.7a, and control points along these sections are displaced. Geometry changes between the sections are obtained through interpolation. As a consequence, the framework is more successful at weakening the mid-chord shock. The progression of the optimizer towards a minimum, as indicated by the convergence plots, weakening of the shock on the wing, and the good agreement in the final optimized values of the aerodynamic coefficients

Table 3.3: Comparison of computed Onera M6 C_D, C_L and C_M values with those from ECARP

	C_D	C_L	C_M
ECARP Baseline	0.0124	0.2828	0.0058
ASO Framework Baseline	0.0128	0.2899	0.0058
ECARP Optimized Case 1	0.0094	0.2832	0.0057
ECARP Optimized Case 2	0.0095	0.2824	0.0057
ASO Framework Optimized	0.0097	0.2898	0.0058

are encouraging, demonstrating that the framework can successfully conduct constrained optimization of 3D geometry.

3.3 Synthesis

OWN studies 1-3 are based on the building blocks presented in this section and developing the capability required to conduct these studies was a major component of this project. STAR-CCM+ was used because it is commercially supported and has all the elements necessary for shape optimization, however, additional development effort was needed to create an ASO framework that linked the CFD solver to an optimizer. Validating the developed models and the framework was critical, as it would lend support to the credibility of the results from subsequent studies. It was important that the CFD models captured the correct physics, and that the ASO framework worked as intended, and significant effort was expended to this effect. The validation process yielded useful insight into the capabilities and limitations of the available tools, also providing valuable lessons to take forward. In the end, it was a success: both the models and the framework were validated, albeit within small discrepancies that were deemed acceptable. The authors are confident that the developed tools work as intended and the baseline models are capturing the correct physics.

Chapter 4

Study 1: Simple Nacelle Sweep

4.1 Formulation

The primary objective of this study is to establish a preliminary trend for total C_D vs. nacelle X/c location for the OWN concept. The goal is to gain insight into the physics of the design space, understanding the prominent flow features for each nacelle location, and their impact on the total drag of the wing-body-nacelle combination. This study uses a non-optimized wing-body in conjunction with a non-optimized through flow nacelle. The location of the nacelle for each case is shown in Table 4.1. The reference point is at the centre of the inlet plane. Negative X/c values imply that the nacelle inlet is ahead of the wing LE. In order to match C_L, each case is run at $\alpha = \{2, 4\}$ deg from which linear regression is used to find C_{L_α}, C_{L_0}, α_{match}.

The secondary objective of this study is to ascertain the appropriateness of using a fixed mesh for varying nacelle locations. While the validated mesh, discussed in the preceding section, adequately captures the flow features for the baseline wing-body configuration, adding an over-wing nacelle and changing its location will result in vastly different flow fields. In particular, the location of shocks and regions of flow separation will be different for each case. While a fixed mesh may not be able to resolve complex flow features to the same level of accuracy as an adapted mesh, a good fixed mesh will still be able to capture the correct trends, albeit with a small error in the values. To determine that this is indeed the case, results obtained from the validated trimmer mesh are compared to those obtained from an adaptively refined mesh for each nacelle location. Figs. 4.1a and 4.1b present an example of the meshes for trial 1.

Table 4.1: Study 1 Nacelle Locations at Mach 0.85, $C_L = 0.5$ ($c = 7.96\ m,\ w = h = 3.80\ m$).

Case	X/c	Y/w	Z/h	α_{fixed}	$\alpha_{adapted}$
1	−0.62	2.54	1.88	2.36	1.97
2	−0.44	2.54	1.88	3.17	2.25
3	−0.26	2.54	1.88	3.69	2.73
4	−0.08	2.54	1.88	3.24	2.69
5	0.10	2.54	1.88	3.56	2.98
6	0.28	2.54	1.88	4.33	3.28
7	0.46	2.54	1.88	3.85	3.54
8	0.64	2.54	1.88	3.87	3.64
9	0.82	2.54	1.88	3.95	3.75
10	1.00	2.54	1.88	3.52	3.34

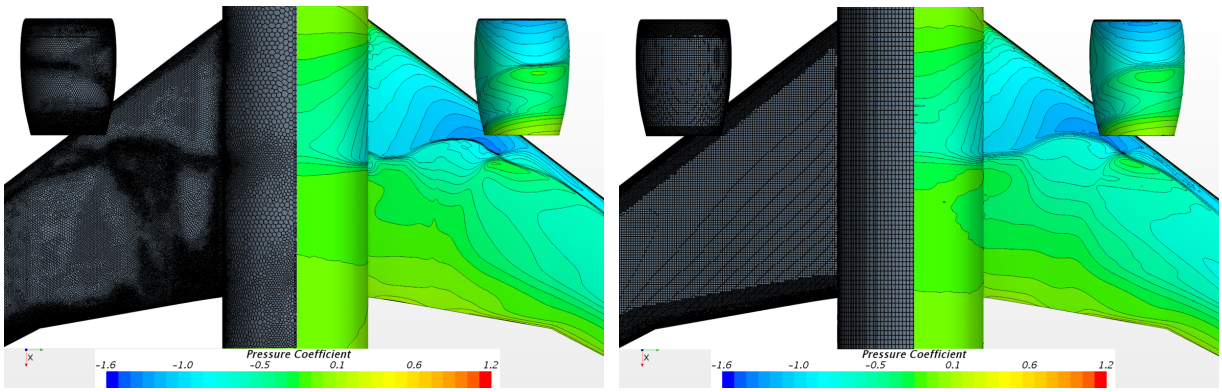

(a) Adapted Mesh

(b) Fixed Mesh

Figure 4.1: Adapted mesh vs. fixed mesh for OWN case 1

4.2 Results

4.2.1 Preliminary Trends

Figure 4.2 compares the C_D trends for the fixed and adapted mesh. In addition to the total C_D, trends for the wing-body C_D and nacelle C_D are also shown. The red line in the figure depicts the drag for the baseline CRM wing-body at $\alpha = 2$ deg, and serves as a reference for comparison purposes. Figures 4.4-4.6 show detailed flow features for cases 1, 6 and 10 respectively. Figure 4.3 shows a 2D snapshot of the flow field for cases 1-10, for both the fixed and adapted mesh. Differences in the flow features captured by the two mesh types are discussed in the following section.

At OWN LE positions, the presence of the nacelle results in greater flow acceleration over the wing LE, resulting in a larger suction peak relative to the clean wing, as seen in Fig. 4.4. This results in a smaller component of the force in the axial direction. This mechanism can help counteract the increased drag penalty due to the stronger shock near the wing LE. As the nacelle is moved further aft over the wing, the shock induced by the flow acceleration between the nacelle and wing is strong enough to cause significant flow separation, as seen in Figs. 4.5 and 4.3. This leads to an increase in the wing-body drag. The back pressure created by nacelle results in a much stronger shock on the wing, which is further upstream than in the clean case. There is also an interaction between the shock induced by the nacelle and the shock on the outboard section of the wing. In general, interference drag penalties are far more pronounced in this region resulting in a higher drag relative to the LE and TE cases. At OWN TE positions, seen in Fig. 4.6, the combination of the nacelle induced back pressure and the higher angle of attack required to match lift, results in a larger beneficial suction region near the wing LE, however at the cost of a strong shock. A second shock is observed at outboard wing regions as a result of this wing-nacelle interaction. Flow separation is not as pronounced as before, and hence the wing-body drag drops as the nacelle is moved further aft. Additionally, nacelle drag decreases due to the larger suction region at the nacelle lower lip caused by increased flow acceleration.

While it is early to draw definitive conclusions regarding the feasibility of the OWN concept relative to the UWN case, the OWN LE and TE cases do however show promise and are valid candidates for further exploration. OWN LE positions use the wing to shield jet noise, thereby reducing the takeoff noise footprint, while OWN TE positions use the wing to shield the fan noise, reducing the approach noise impact. Additional aerodynamic benefits are likely at these positions once the nacelle and wing shocks are weakened through shape optimization. It does however seem unlikely that for the 'middle' OWN cases, optimization will be able to resolve the interference penalties to a sufficient degree.

4.2.2 Mesh Sensitivity Analysis

While the trends captured by the fixed and adapted meshes as seen in Fig. 4.2 are similar, there are differences in the C_D values, which are to be expected. These differences can be explained by comparing at the flow features seen in Fig. 4.3. In cases 2, 8 and 9 for example, the fixed mesh quite clearly over-predicts

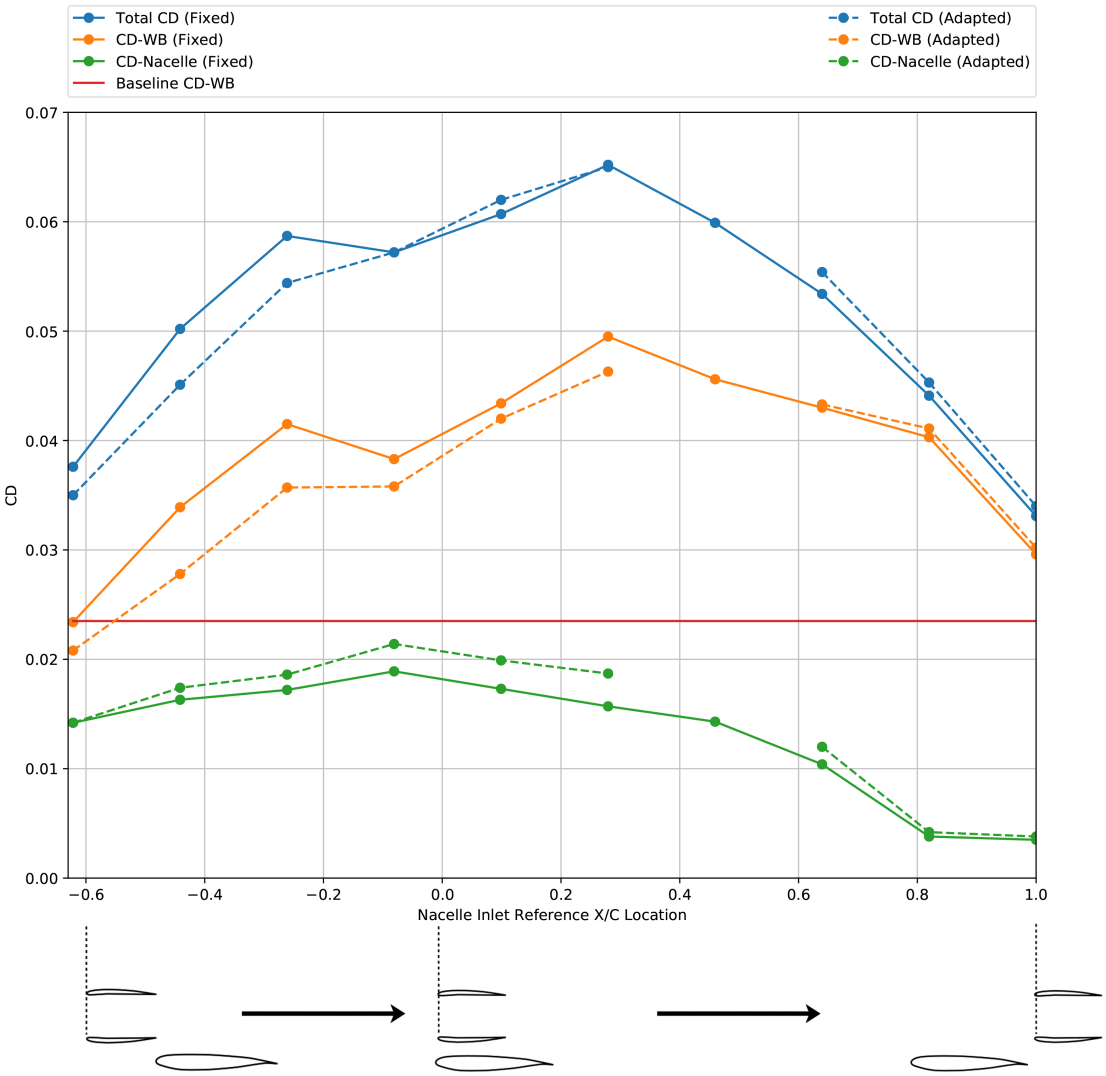

Figure 4.2: Variation of C_D with nacelle X/C location at Mach 0.85, $C_L = 0.5$

flow separation over the wing, while in case 6 flow separation behind the shock on the nacelle upper surface of the nacelle is over-predicted. Additionally, in cases 4-6 for example, the shock on the nacelle upper surface is clearly better resolved than in the fixed case. In general, the better resolved the shock on the nacelle upper surface accounts for the higher nacelle drag predicted by the adapted mesh, whereas, the over-predicted flow separation over the wing accounts for the larger wing-body drag predicted by the fixed mesh. These differences are prominent for OWN LE and 'middle' cases. Errors in the wing-body and nacelle drag values cancel to a certain extent, resulting in a smaller difference in the total drag prediction by the two meshes.

4.3 Synthesis

This study conducted an over-wing nacelle sweep along the x direction to gain preliminary insight into the C_D trend vs. nacelle position for a non-optimized wing-body and nacelle. Additionally, sensitivity of the results to the mesh resolution was assessed by comparing the results obtained by a fixed mesh, to those obtained from a mesh adaptively refined for each nacelle location. The C_D trend suggests that OWN LE and TE positions are more favorable than 'middle' positions, and that both are comparable in terms of total C_D. The

flow field analysis reveals that placing the nacelle over the wing results in greater flow acceleration between the nacelle and the wing, which can lead to a second shock and flow separation for some locations. OWN LE positions are characterized by a larger beneficial suction peak on the wing only, and while the wing shock is weaker, a secondary shock is observed. OWN TE positions are characterized by a larger back pressure on the wing due to the nacelle, resulting in a strong shock that terminates earlier. There is however a beneficial suction peak on both the nacelle and wing that somewhat counteracts the wave drag penalty due to the stronger shock. Both LE and TE positions show interesting features that warrant further exploration, and show potential for being feasible design upon shape optimization. Lastly, the mesh sensitivity comparison shows good agreement between the fixed and adapted meshes in terms of the drag trend. The fixed mesh is adequate in capturing the important flow features like the shock location and regions of flow separation, however, it lacks refinement to resolve them to the same level of accuracy as an adapted mesh. Nevertheless, a fixed mesh is sufficient for design space exploration purposes, where the emphasis is on obtaining accurate trends as efficiently as possible.

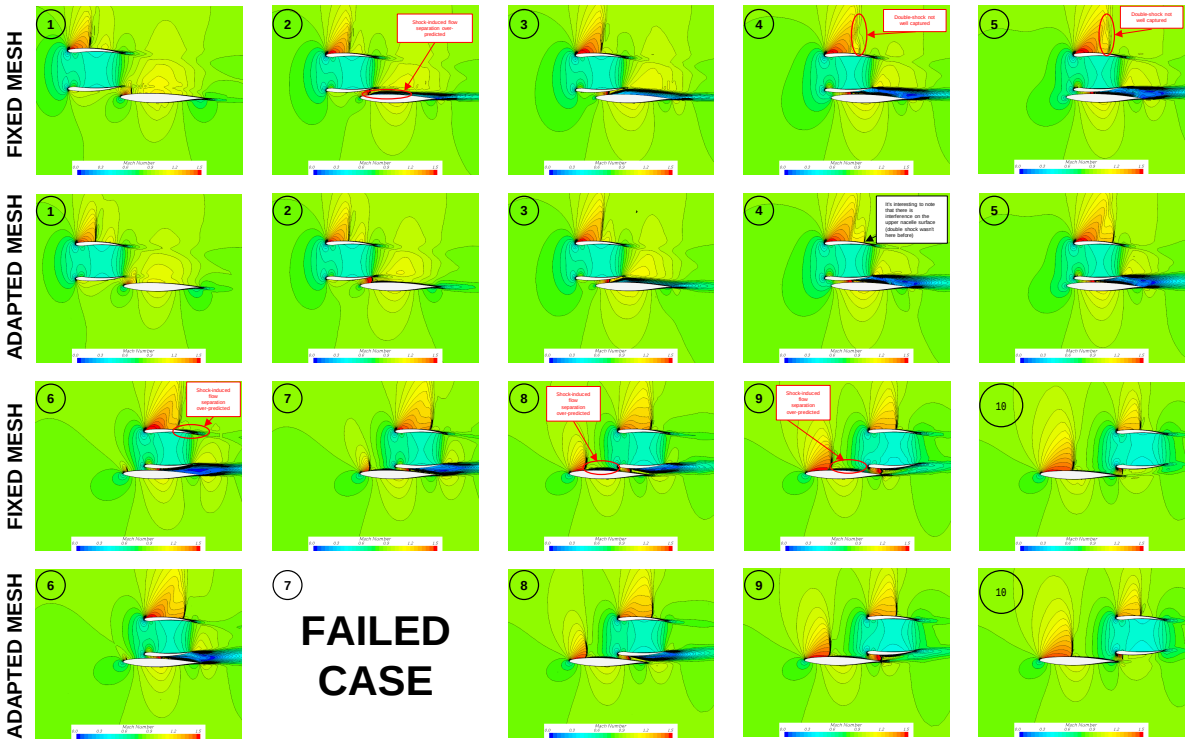

Figure 4.3: Flow features for cases 1–10: Fixed mesh vs. Adapted mesh

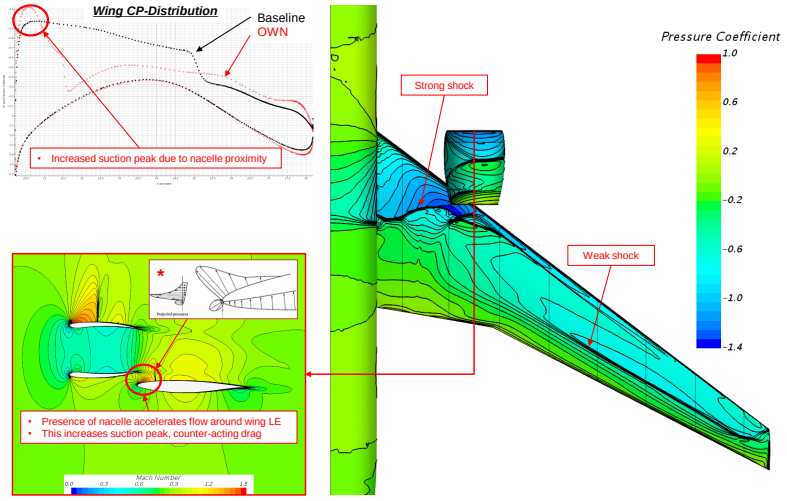

Figure 4.4: Detailed Flow Analysis: Case 1

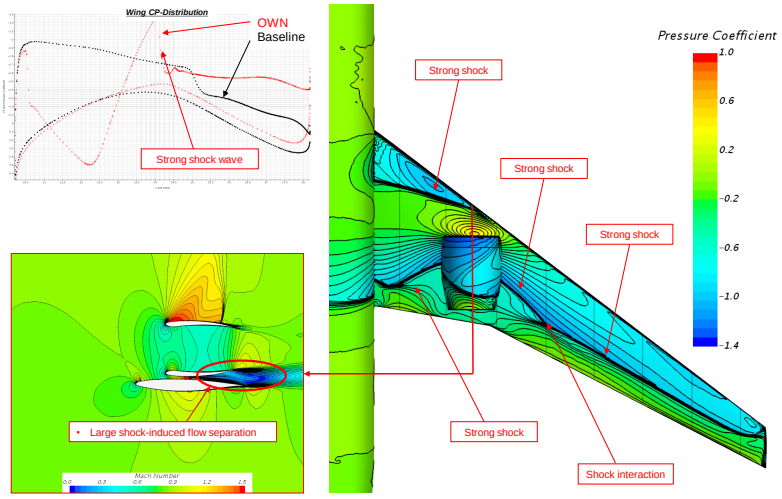

Figure 4.5: Detailed Flow Analysis: Case 6

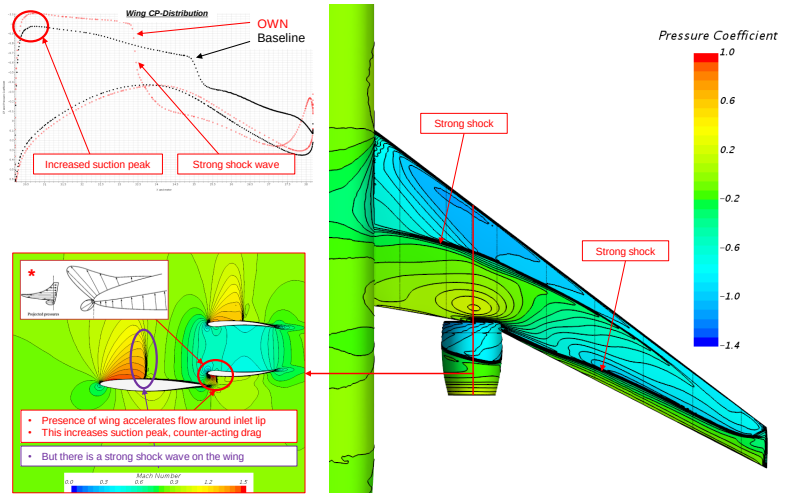

Figure 4.6: Detailed Flow Analysis: Case 10

Chapter 5

Study 2: OWN Sensitivity Analysis

Numerical Propulsion-Airframe Integration (PAI) studies usually adopt a decoupled solution method, in which the effect of the engine on the flow field is accounted for through the application of powered boundary conditions in CFD, but the effect of airframe aerodynamics on the engine is not. The need to account for such coupling is obvious for certain applications like Boundary Layer Ingestion (BLI) engines [20], but perhaps less so for podded nacelle configurations such as Over-Wing Nacelles (OWN) concepts. The development of OWN such as the Boeing YC-14 [11] is historically tied to Upper Surface Blowing (USB) technology for Short Takeoff and Landing (STOL) applications where leading-edge, slipper-mounted engines generate powered lift by blowing hot exhaust over the top surface of the wing to take advantage of the Coandă effect; a highly coupled, multi-disciplinary problem. However, modern applications such as the Lockheed HWB [4] have shifted the paradigm from "design for STOL" to "design for energy efficiency" using trailing-edge, podded engines configuration, likely to exhibit weaker aero-propulsive coupling; but how much weaker?

The purpose of this study is to quantify the strength of aero-propulsive coupling for podded OWN. This will be accomplished using statistical analysis to quantify the sensitivity of powered effects on installation drag, engine pressure recovery, and lift curve characteristics at cruise as a function of nacelle XYZ location and power setting. All data is generated using the Reynolds Averaged Navier-Stokes (RANS) equations with a validated CFD model of the NASA Common Research Model [6] (CRM), modified with over-wing engines. The rest of this chapter is organized as follows: the next section describes the general methodology used for sensitivity analysis, followed by a more specific description of the experiment, results, and synthesis.

5.1 Mathematical Approach

Multi-Disciplinary Analysis (MDA) captures inter-disciplinary coupling; but it is complex and computationally expensive. Hence, it makes sense to first test for strong inter-disciplinary coupling before deciding to invest the resources. Indeed, one need not solve an MDA to quantify the strength of aero-propulsive coupling; so-called effects screening can be used to that end. The method uses *screening experiments* from the field of Design Of Experiments (DOE), *linear regression*, and *Analysis of Variance* (ANOVA) to test for the significance main effects and two-factor interactions [21, 22]. Hence, in order to test for the presence of strong aero-propulsive coupling, it suffices to statistically quantify the significance of any interaction between the two disciplines. If no significant interaction exists, then the coupling is weak. This section explains the theory used to accomplish this following the development by Hines et al. [21]

5.1.1 Statistical Analysis

Consider the general linear regression model given by,

$$y = f(\boldsymbol{x}) = \sum_{j=1}^{m} \beta_j \phi_j(\boldsymbol{x}) + \epsilon \quad \text{where} \quad \epsilon \sim \mathcal{N}(0, \sigma^2) \tag{5.1}$$

where $f \in \mathbb{R}$ is some deterministic function of interest, $\boldsymbol{x} \in \mathbb{R}^p$ is a vector of standardized design variables, β_j are unknown regression coefficients to be found and ϕ_j is some assumed basis function associated with the j^{th} coefficient. This model assumes that the residual error ϵ is Gaussian. This error could be the result of true random variation in a stochastic process or, small deterministic error that appears random due to the assumed form of the model (*i.e.* the assumed model does not exactly capture the response but it is close), or both. The magnitudes of the coefficients β_j are indicative of the relative importance of a given basis function ϕ_j. Consider a dataset of N samples,

$$\begin{pmatrix} y_1 \\ \vdots \\ y_N \end{pmatrix} = \begin{pmatrix} \phi_1(\boldsymbol{x}_1) & \dots & \phi_m(\boldsymbol{x}_1) \\ \vdots & \ddots & \vdots \\ \phi_1(\boldsymbol{x}_N) & \dots & \phi_m(\boldsymbol{x}_N) \end{pmatrix} \begin{pmatrix} \beta_1 \\ \vdots \\ \beta_m \end{pmatrix} \quad \Leftrightarrow \quad \boldsymbol{y} = \boldsymbol{X}\boldsymbol{\beta} \tag{5.2}$$

where $\boldsymbol{y} \in \mathbb{R}^N$, $\boldsymbol{X} \in \mathbb{R}^{N \times m}$ and $\boldsymbol{\beta} \in \mathbb{R}^m$. Under the standard setting where $N > m$, the solution to Eq. 5.2 is usually obtained using the Least Squares Estimator (LSE):

$$\hat{\boldsymbol{\beta}} = \arg\min_{\boldsymbol{\beta} \in \mathbb{R}^m} L \quad \text{where} \quad L = (\boldsymbol{y} - \boldsymbol{X}\boldsymbol{\beta})'(\boldsymbol{y} - \boldsymbol{X}\boldsymbol{\beta}) = \sum_{i=1}^{N} \left(y_i - \sum_{j=1}^{m} \beta_j \phi(x_{ij}) \right)^2 \tag{5.3}$$

This can be solved in two ways: optimization or using the normal equations. Using the latter, taking the partial derivatives with respect to β_j, and setting to zero, one obtains a linear system of m equations:

$$\left. \frac{\partial L}{\partial \boldsymbol{\beta}} \right|_{\hat{\boldsymbol{\beta}}} = -2\boldsymbol{X}'\boldsymbol{y} + 2\boldsymbol{X}'\boldsymbol{X}\hat{\boldsymbol{\beta}} = \boldsymbol{0} \tag{5.4}$$

The solution to these so-called normal equations is given by:

$$\hat{\boldsymbol{\beta}} = (\boldsymbol{X}'\boldsymbol{X})^{-1}\boldsymbol{X}'\boldsymbol{y} \tag{5.5}$$

Statistical Properties

Note that the least squares estimator in Eq. 5.5 is a random vector, since ϵ is Gaussian,

$$\hat{\boldsymbol{\beta}} = (\boldsymbol{X}'\boldsymbol{X})^{-1}\boldsymbol{X}'(\boldsymbol{X}\boldsymbol{\beta} + \epsilon) \tag{5.6}$$

and, moreover, it is Gaussian itself since a linear combination of Gaussian terms is still Gaussian. Applying definitions of mean and covariance, it can be shown that $\hat{\boldsymbol{\beta}}$ is an unbiased estimator of $\boldsymbol{\beta}$, with parameters:

$$\mathbb{E}(\hat{\boldsymbol{\beta}}) = \boldsymbol{\beta} \tag{5.7}$$

$$\text{Cov}(\hat{\boldsymbol{\beta}}) = \sigma^2(\boldsymbol{X}'\boldsymbol{X})^{-1} \tag{5.8}$$

It is necessary to estimate σ^2. To do so, re-write the sum of squares of the residuals in Eq. 5.3 as:

$$SS_E = |\boldsymbol{y} - \boldsymbol{X}\boldsymbol{\beta}|_2^2 = (\boldsymbol{y} - \boldsymbol{X}\hat{\boldsymbol{\beta}})'(\boldsymbol{y} - \boldsymbol{X}\hat{\boldsymbol{\beta}}) = \boldsymbol{y}'\boldsymbol{y} - \hat{\boldsymbol{\beta}}'\boldsymbol{X}'\boldsymbol{y} \tag{5.9}$$

All the terms in this equation are known, since they can be calculated from the data. There are $N - m$ degrees of freedom, which represents the number of data samples available beyond the minimum necessary. Hence, the mean square error is given by:

$$MS_E = \frac{SS_E}{N - m} \tag{5.10}$$

Others have shown that the expected value of MS_E is σ^2; hence, an unbiased estimator of σ^2 is given by

$$\hat{\sigma}^2 = MS_E \tag{5.11}$$

Hypothesis Testing on Individual Regression Coefficients

The hypotheses for testing the significance of any individual regression coefficient β_j is:

$$\text{H0:} \quad \beta_j = 0, \tag{5.12}$$

$$\text{H1:} \quad \beta_j \neq 0. \tag{5.13}$$

Recall that individual coefficients are distributed as $\hat{\beta}_j \sim \mathcal{N}(\beta_j, \sigma^2 C_{jj})$ where C_{jj} is the diagonal element of $(\boldsymbol{X}'\boldsymbol{X})^{-1}$ in Eq. 5.7. Hence, under the null hypothesis, the quantity t_0 follows a student-t distribution:

$$t_0 = \frac{\hat{\boldsymbol{\beta}}_{\boldsymbol{j}}}{\sqrt{\hat{\sigma}^2 C_{jj}}} \tag{5.14}$$

The null hypothesis H0: $\beta_j = 0$ would thus be rejected at the $1 - \alpha$ confidence level if $|t_0| > t_{\alpha/2,N-m}$. Alternatively, this result is often expressed as a p-value, which expresses the probability that the observed value of t_0 is greater than what it should be under the null hypothesis:

$$p = P\left(|t_0| > t_{\alpha/2,N-m} | H0\right) \tag{5.15}$$

If $p \leq 0.05$, then this is usually a strong indicator that β_j is statistically significant; otherwise, it can be dropped from the model. In the case of effects screening, where β_j multiplies main effects x_j, the latter implies that x_j contributes little to the response and can thus be defaulted to some fixed value. Once t_0 has been established for each coefficient, the "vital few" can be separated from the "trivial many." One popular method is Lenth's Pseudo Standard Error (PSE) [**?**], which describes a repeatable process for determining the decision threshold; the reader is referred to the literature for more detail.

5.1.2 Concept Behind Effects Screening

With this background in place, the concept behind effect screening can now be explained. It proceeds by sampling the extremes of the design space, using specialized sampling plans known as screening designs, followed by statistical regression. The idea is to choose the basis functions ϕ_j such that they are functions of only specific design variables (i.e. $\phi_j(\boldsymbol{x}) = \phi_j(x_j)$). In the methods by Myers and Montgomery [23], the basis functions are taken to form a linear model containing main effects and two-factor interactions only,

$$f = \beta_0 + \underbrace{\sum_{i=1}^{p} \beta_i x_i}_{\text{main effects}} + \underbrace{\sum_{i=1}^{p-1} \sum_{j=i+1}^{p} \beta_{ij} x_i x_j}_{\text{two-factor interactions}} \tag{5.16}$$

As a result, the magnitude of the coefficients β_i indicate the relative importance of the main effects x_i and β_{ij} indicate the relative importance of the two-factor interactions $x_i x_j$. Higher-order interactions are neglected under the sparsity-of-effects principle (also known as the Pareto principle), which is based on the observation that in most engineering problems the response is only driven by a small number of main effects and second-order interactions [23].

Constructing the Sampling Plan

Up to now, the methodology has explained how to use a given set of data in order to draw conclusions about the importance of main effects; but how should this data be generated in the first place? Screening designs stem from the field of designs of experiment. They seek to maximize information about the design space, while minimizing the number of samples needed for an assumed statistical model. For instance, the minimum number of samples needed to regress Eq. 5.16 is obtained by counting the number of regression coefficients β:

$$N_{min} = 1 + p + p(p-1)/2 \tag{5.17}$$

Table 5.1: Example of a 2^{3-1} factorial design

Treatment No.	x_1	x_2	x_3	y
τ_1	+	+	−	$y^{(1)}$
τ_2	+	−	+	$y^{(2)}$
τ_3	+	−	−	$y^{(3)}$
τ_4	+	+	+	$y^{(4)}$
τ_5	+	+	+	$y^{(5)}$
τ_6	+	+	−	$y^{(6)}$
τ_7	+	−	+	$y^{(7)}$
τ_8	+	−	−	$y^{(8)}$

For large design spaces ($p \gg 10$), this number can be large, which defeats the purpose of screening. However, it can be reduced if terms are grouped together in a concept known as aliasing [23]. For example, a three-variable model can be reduced from $2^3 = 8$ coefficients to $2^{3-1} = 4$ by aliasing main effects and two-factor interactions:

$$f = \beta_0 + \beta_1 \underbrace{(x_1 + x_2 x_3)}_{\text{aliased}} + \beta_2 \underbrace{(x_2 + x_1 x_3)}_{\text{aliased}} + \beta_3 \underbrace{(x_3 + x_1 x_2)}_{\text{aliased}} \tag{5.18}$$

The only disadvantage is that it is no longer possible to tell main effects x_i apart from two-factor interactions $x_j x_k$, since the magnitude of β_j only provides information about the group $x_i + x_j x_k$. The ability to distinguish main effects apart from interactions is a property known as resolution [23]. It is determined by the sampling plan, which are typically chosen to be fractional factorial designs of resolution III and IV [23] or Plackett-Burman designs [24]:

- **Resolution III designs** are designs in which no main effects are aliased with any other main effect, but main effects are aliased with two-factor interactions, and two-factor interactions may be aliased with each other.
- **Resolution IV designs** are designs in which no main effects are aliased with any other main effect or with any two-factor interaction, but two-factor interactions may be aliased with each other.
- **Resolution V designs** are designs in which no main effects or two-factor interactions are aliased with any other main effect or with any two-factor interaction.

An example of a resolution IV fractional factorial design is given in Table 5.1. Treatments $\tau_1, \ldots, \tau_8$ represent the full factorial, whereas treatments $\tau_1, \ldots, \tau_4$ represent the fractional factorial. As can be seen, these types of screening designs assume only two levels for each factor, denoted by the "+" and "−" symbols, corresponding to the maximum ($x_{i,max}$) and minimum ($x_{i,min}$) bounds of the design space, respectively. Skipping over much of the theory behind design of experiments, this design yields the following alias structure,

$$x_1 = x_2 x_3 \qquad x_2 = x_1 x_3 \qquad x_3 = x_1 x_2 \tag{5.19}$$

which agrees with Eq. 5.18. In other words, treatments $\tau_1, \ldots, \tau_4$ in Table 5.1 is the minimum screening design required to regress Eq. 5.18.

Note that if one wished to resolve all terms, as in Eq. 5.20, then one would have to run the full factorial $\tau_1, \ldots, \tau_8$. Adding more data always increases resolution, but care must be taken to keep the design balanced. Mathematically, this means there must always be an equal number of "+" and "−" in each column of Table 5.1. In other words, this means that for a given design resolution, the model must not be biased due to uneven sampling of the design space. Hence, increasing resolution is always achieved by "folding over" the design, as illustrated in Table 5.1, which increases the number of runs required by a factor of two every time.

$$f = \beta_0 + \beta_1 x_1 + \beta_2 x_2 + \beta_3 x_3 + \beta_{23} x_{23} + \beta_{13} x_{13} + \beta_{12} x_{12} \tag{5.20}$$

5.2 Design of Experiment

Now that the general theory behind *effect screening* in place, it can be applied to the problem at hand. The factors, responses, and design of experiment selected for this study are shown in Table 5.2, where the raw data used for analysis in Section 6.3 has been included. The DOE consists of a fractional factorial design of resolution V augmented with baseline runs, where each treatment $(\tau_1, \ldots, \tau_{22})$ was evaluated using the modeling and simulation environment described in section 3.1. The following subsections will now define the quantities associated with each column in Table 5.2.

Table 5.2: Raw data at $C_L = 0.5$, M= 0.85, $alt = 10,668\ m$ ($c = 7.96\ m,\ w = h = 3.80\ m$). *In order to match C_L, each case was run at $\alpha = \{0, 2, 4\}$ deg from which linear regression was used to find C_{L_α}, C_{L_0}, α_{match}.*

Treatment	$\Delta X/c$	$\Delta Y/w$	$\Delta Z/h$	Config	PC	ΔC_{L_α}	ΔC_{L_0}	ΔC_D	ΔPR
	–	–	–	–	–	$10^{-4} \cdot deg^{-1}$	10^{-4}	10^{-4}	%
τ_1	−0.20	−0.35	0.30	LE	50	-110	80.0	19	2.00
τ_2	+0.30	+0.35	0.00	TE	50	140	-1140	32	0.91
τ_3	+0.30	−0.35	0.00	LE	50	-280	-910	357	0.07
τ_4	−0.20	−0.35	0.00	TE	50	80	-1980	269	2.27
τ_5	−0.20	+0.35	0.00	LE	50	-100	240	16	0.01
τ_6	−0.20	+0.35	0.30	TE	50	-100	-1600	326	0.15
τ_7	+0.30	−0.35	0.30	TE	50	70	-970	21	0.14
τ_8	+0.30	−0.35	0.00	TE	40	130	-1110	21	0.38
τ_9	+0.30	−0.35	0.30	LE	40	-350	-590	36	0.04
τ_{10}	−0.20	+0.35	0.00	TE	40	-220	-1970	406	0.39
τ_{11}	−0.20	−0.35	0.30	TE	40	-50	-2100	305	0.34
τ_{12}	−0.20	−0.35	0.00	LE	40	-260	210	107	0.02
τ_{13}	+0.30	+0.35	0.00	LE	40	-380	-320	300	0.02
τ_{14}	+0.30	+0.35	0.30	LE	50	-430	100	276	0.02
τ_{15}	−0.20	+0.35	0.30	LE	40	60	-20	0	0.00
τ_{16}	+0.30	+0.35	0.30	TE	40	140	-1280	45	0.27
τ_{17}		Baseline		TE	40	120	-2100	99	2.50
τ_{18}		Baseline		TE	44	130	-1960	89	2.29
τ_{19}		Baseline		TE	50	-400	120	77	1.92
τ_{20}		Baseline		LE	40	-410	130	206	0.00
τ_{21}		Baseline		LE	44	-420	170	207	0.05
τ_{22}		Baseline		LE	50	-100	-1600	216	0.00

5.2.1 Definition of Factors

The five factors are the relative nacelle displacements (ΔX, ΔY, ΔZ), configuration type, and engine Power Code (PC). Their definitions are provided in Fig. 6.1. For convenience, a distinction was made between Leading Edge (LE) and Trailing Edge (TE) configurations such that the Δ's are always expressed relative to a local coordinate system that depends on the configuration type, as shown in Fig. 5.1a. Note that the local X-axis is reversed for the TE baseline to ensure that $+\Delta X$ is always towards the wing and $-\Delta X$ is always a away from it. Beyond engine displacement, changing the power setting is a way to test the strength of the aero-propulsive coupling. Indeed, if airframe aerodynamics are sensitive to changes in the engine's boundary conditions, then artificially changing the engine's power code is a way to find out; otherwise, the coupling is weak. Fig. 5.1b shows the baseline engine's power hook and the selected range of power codes (*i.e.* power codes 40 – 50).

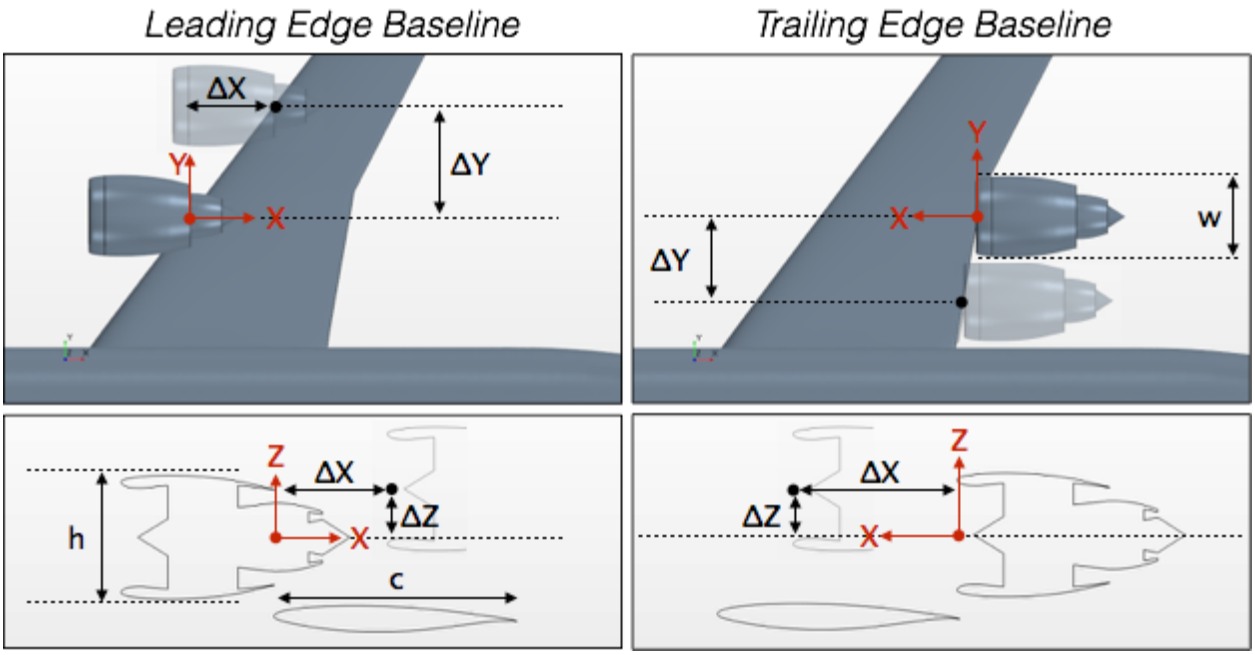

(a) Definition of relative displacements and configuration type

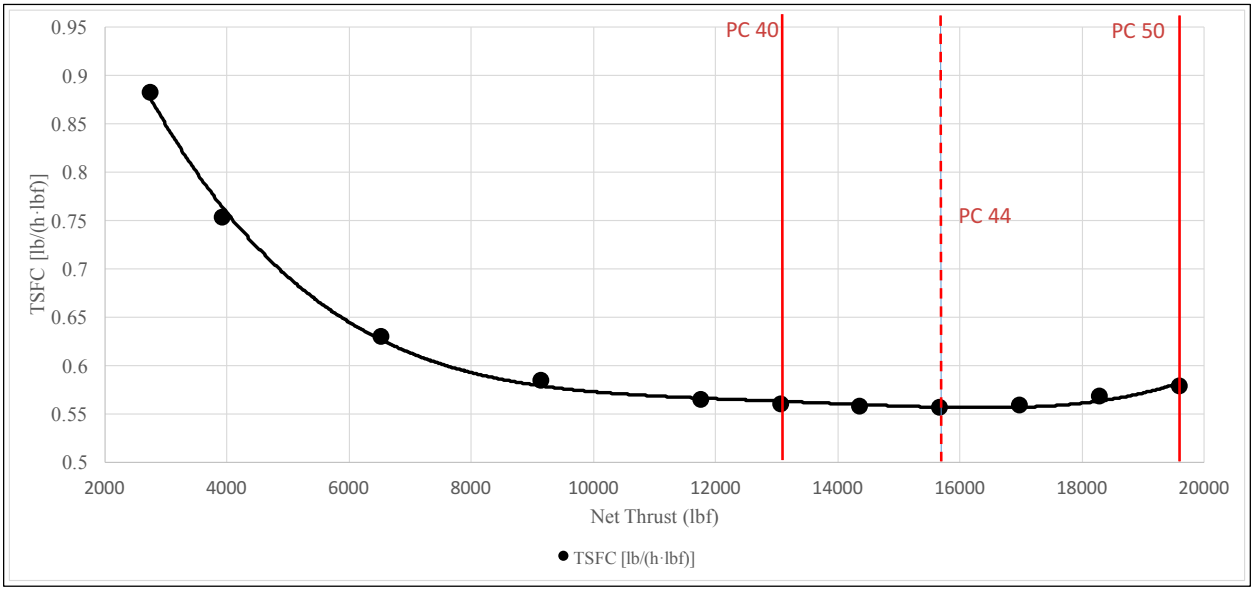

(b) Selected power code range of variation for notional high bypass turbofan of 94,000 lb thrust class

Figure 5.1: Definition of the factors varied in the experiment

5.2.2 Definition of Responses

The four responses of interest are: installation drag ΔC_D, change in pressure recovery ΔPR, change in lift curve slope ΔC_{L_α}, and change in lift curve intercept ΔC_{L_0}. This subsection will now define them clearly.

Installation Drag

When the engine is brought into close proximity of the wing-body, the flow field of the former interacts with the flow field of the latter, possibly resulting in excess drag beyond that of the isolated bodies. This is

termed installation drag and can thus be decomposed into two components: (i) the change in drag on the wing-body due to the presence of a nacelle and (ii) the change in drag on the nacelle due to integration with the wing-body. However, since installing an engine onto a clean wing changes the effective angle of attack, care must be taken to compute installation drag at a constant C_L. In the definition that follows, the notation $(C_{D,x})^y_z$ denotes drag coefficient computed on the surface x (*i.e.* wing-body, nacelle) of the configuration y (*i.e.* wing-body-nacelle, wing-body, isolated-nacelle) at constant z (*i.e.* C_L). The installation drag is denoted by Δ according to:

$$\Delta\left(C_{D_{WB}}\right)^{WBN}_{C_L} = \left(C_{D_{WB}}\right)^{WBN}_{C_L} - \left(C_{D_{WB}}\right)^{WB}_{C_L} \tag{5.21}$$

$$\Delta\left(C_{D_N}\right)^{WBN}_{C_L} = \left(C_{D_N}\right)^{WBN}_{C_L} - \left(C_{D_N}\right)^{N}_{C_L=0} \tag{5.22}$$

$$\Delta C_D \equiv \Delta\left(C_{D_{WBN}}\right)^{WBN}_{C_L} = \left(\Delta C_{D_N}\right)^{WBN}_{C_L} + \left(\Delta C_{D_{WB}}\right)^{WBN}_{C_L} \tag{5.23}$$

Inlet Pressure Recovery

The inlet pressure recovery (PR) is defined as the ratio of total pressures at the fan-face (P_{t2}) and the freestream (P_{t0}). Under ideal conditions, this ratio is 1 but non-isentropic losses can cause this number to drop. Let the change in pressure recovery due to engine installation be defined as:

$$\Delta PR = \left(\frac{P_{t2}}{P_{t0}}\right)_{Isolated-N} - \left(\frac{P_{t2}}{P_{t0}}\right)_{WBN} \tag{5.24}$$

Lift Curve Parameters

Let the parameters $C_{L\alpha}$ and C_{L0} denote the lift curve slope and intercept, respectively, and let $(C_{L_x})^y$ denote the parameter x (*i.e.* C_{L_α} or C_{L_0}) computed on the configuration y (*i.e.* wing-body-nacelle or isolated wing-body). The change in parameters due to engine installation is then given by:

$$C_L = C_{L_0} + \alpha\ C_{L\alpha} \tag{5.25}$$

$$\Delta C_{L_0} = \left(C_{L_0}\right)^{WBN} - \left(C_{L_0}\right)^{WB} \tag{5.26}$$

$$\Delta C_{L_\alpha} = \left(C_{L_\alpha}\right)^{WBN} - \left(C_{L_\alpha}\right)^{WB} \tag{5.27}$$

5.3 Results

Sensitivity analysis results are presented in Fig. 5.2 using the method described in Section 5.1, applied to each response. In the material to follow, the reader should interpret sensitivities in a relative sense, *i.e.* "relative to the effect of variable A, the effect of B is less (more) significant."

5.3.1 Airframe Installation Drag

The sensitivity analysis results for installation drag (ΔC_D) are shown in Fig. 5.2a. The magnitude of the bar indicates importance, while direction indicates whether the response increases or decreases with respect to that effect. The p-values are statistical measures of significance; smaller means more significant. The cutoff p-value was taken to be 0.05, meaning that all results are reported with 95% confidence. It can be seen that chord-wise placement (ΔX) is by far the most dominant effect. However, configuration type (TE/LE), and the interaction of configuration type with ΔX, ΔY, and ΔZ also influence the response with statistical significance. Each one will now be explained in more detail. No attempt was made to re-optimize airfoil shapes in this study; analysis holds for a fixed outer mold line.

Effect of ΔX on ΔC_D

The primary reason why this effect is so significant is that chord-wise placement drives the strength and location of the shock waves. This is known from previous work [25] and illustrated in Fig. 5.3 for two

Term	Contrast		Lenth t-Ratio	Individual p-Value
Δx	0.012462		22.51	<.0001*
TE/LE	0.001700		3.07	0.0123*
PC	-0.001144		-2.07	0.0520
Δy	-0.000309		-0.56	0.5891
Δz	-0.000124		-0.22	0.8226
Δx*Δx	0.001559	*	2.82	0.0182*
Δx*TE/LE	-0.000192		-0.35	0.7329
Δx*PC	-0.000309		-0.56	0.5891
TE/LE*PC	0.000296		0.53	0.6068
PC*PC	0.000037	*	0.07	0.9475
Δx*Δy	0.000490		0.89	0.3469
TE/LE*Δy	-0.002367		-4.27	0.0023*
PC*Δy	0.000139		0.25	0.8048
TE/LE*Δz	-0.001682		-3.04	0.0127*
PC*Δz	-0.000429	*	-0.77	0.4078
Δx*Δx*TE/LE	-0.002138	*	-3.86	0.0043*
Δx*TE/LE*PC	0.000789		1.42	0.1523
TE/LE*PC*PC	0.000062	*	0.11	0.9118
Δx*TE/LE*Δy	-0.000821		-1.48	0.1394
TE/LE*PC*Δy	0.000746		1.35	0.1699
TE/LE*PC*Δz	-0.000234	*	-0.42	0.6777

(a) Installation drag, ΔCD

Term	Contrast		Lenth t-Ratio	Individual p-Value
TE/LE	-0.514091		-4.70	0.0016*
Δz	-0.313195		-2.86	0.0167*
Δx	0.082615		0.76	0.4194
Δy	-0.080483		-0.74	0.4310
PC	0.073893		0.68	0.4708
TE/LE*Δz	0.311133		2.84	0.0174*
TE/LE*Δx	-0.071955		-0.66	0.5213
Δz*Δx	-0.069823	*	-0.64	0.5360
Δx*Δx	-0.243936	*	-2.23	0.0415*
TE/LE*Δy	0.069823		0.64	0.5360
Δz*Δy	0.069823	*	0.64	0.5360
Δx*Δy	-0.147641		-1.35	0.1690
TE/LE*PC	-0.070080		-0.64	0.5344
Δz*PC	0.106073	*	0.97	0.3052
PC*PC	-0.016002	*	-0.15	0.8841
TE/LE*Δz*Δx	0.067691	*	0.62	0.5492
TE/LE*Δx*Δx	0.249199	*	2.28	0.0378*
TE/LE*Δz*Δy	-0.067691	*	-0.62	0.5492
TE/LE*Δx*Δy	0.143377		1.31	0.1805
TE/LE*Δz*PC	-0.104166	*	-0.95	0.3126
TE/LE*PC*PC	0.003693	*	0.03	0.9747

(b) Pressure recovery, ΔPR

Term	Contrast		Lenth t-Ratio	Individual p-Value
TE/LE	0.080127		11.45	<.0001*
Δx	-0.028521		-4.08	0.0032*
Δy	0.007307		1.04	0.2745
PC	0.006217		0.89	0.3436
Δz	0.005858		0.84	0.3683
TE/LE*Δx	0.004930		0.70	0.4526
Δx*Δx	0.003999	*	0.57	0.5784
TE/LE*Δy	0.005623		0.80	0.3888
Δx*Δy	0.011721		1.68	0.1006
TE/LE*PC	-0.003642		-0.52	0.6135
Δx*PC	0.000965		0.14	0.8906
Δy*PC	0.007329		1.05	0.2732
PC*PC	0.000289	*	0.04	0.9674
TE/LE*Δz	-0.008487		-1.21	0.2113
PC*Δz	-0.000598	*	-0.09	0.9308
TE/LE*Δx*Δx	-0.017299	*	-2.47	0.0273*
TE/LE*Δx*Δy	0.002638		0.38	0.7129
TE/LE*Δx*PC	-0.001317		-0.19	0.8492
TE/LE*Δy*PC	0.004664		0.67	0.5002
TE/LE*PC*PC	0.000068	*	0.01	0.9936
TE/LE*PC*Δz	0.000527	*	0.08	0.9403

(c) Lift curve intercept, ΔC_{L_0}

Term	Contrast		Lenth t-Ratio	Individual p-Value
TE/LE	-0.016468		-7.60	0.0002*
Δx	-0.009599		-4.43	0.0021*
Δz	0.001475		0.68	0.4668
PC	0.001035		0.48	0.6393
Δy	-0.000645		-0.30	0.7674
TE/LE*Δx	-0.001317		-0.61	0.5566
Δx*Δx	0.001385	*	0.64	0.5346
TE/LE*Δz	0.004124		1.90	0.0681
Δx*Δz	-0.001924	*	-0.89	0.3439
TE/LE*PC	-0.001187		-0.55	0.5966
Δx*PC	0.001850		0.85	0.3610
Δz*PC	-0.004299	*	-1.98	0.0606
PC*PC	-0.000012	*	-0.01	0.9964
TE/LE*Δy	0.002137		0.99	0.2978
Δx*Δy	-0.002385	*	-1.10	0.2525
TE/LE*Δx*Δx	0.004685	*	2.16	0.0459*
TE/LE*Δx*Δz	-0.002489	*	-1.15	0.2334
TE/LE*Δx*PC	-0.001444		-0.67	0.5002
TE/LE*Δz*PC	-0.000383	*	-0.18	0.8608
TE/LE*PC*PC	-0.000062	*	-0.03	0.9796
TE/LE*Δx*Δy	-0.000200	*	-0.09	0.9247

(d) Lift curve slope, ΔC_{L_α}

Figure 5.2: Effect screening

examples. Far away from the wing, interference effects essentially disappear; but close to it, the proximity of the nacelle causes local flow acceleration which results in stronger wave drag and even shock-induced boundary layer separation in some particularly bad cases.

Effect of Configuration Type on ΔC_D

Results show that placing the nacelle at the trailing edge is generally better than placing it at the LE. As shown in Fig. 5.3, the presence of the nacelle at TE locations creates back pressure that strengthens the primary shock on the wing and forces it to terminate early (compared to the clean wing), resulting in a loss of lift. At LE locations, the proximity of the nacelle causes local flow acceleration around the wing leading edge, strengthening the primary shock and also causing it to terminate early with a similar loss of lift. In both cases, C_L must be maintained by increasing the angle of attack, resulting in higher leading-edge suction peak which is beneficial because it creates a component of force acting opposite to drag. Overall, OWN TE configurations seem to be inherently better at enhancing suction peak, while limiting wave drag penalties.

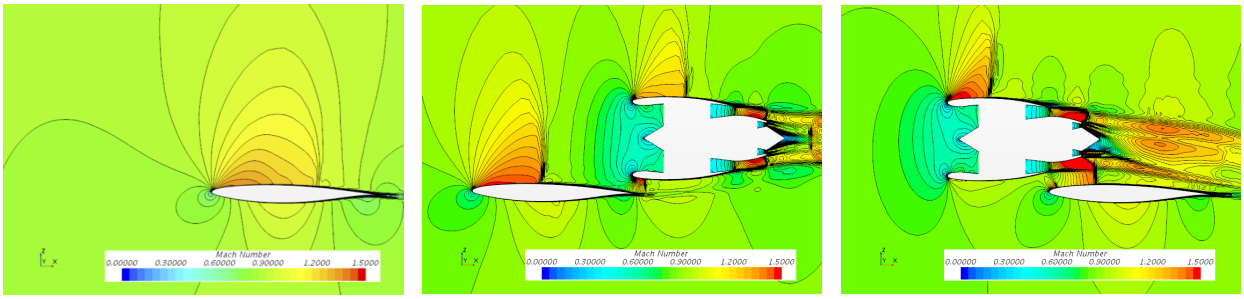

(a) Isolated wing-body (clean wing) (b) Trailing edge baseline (c) Leading edge baseline

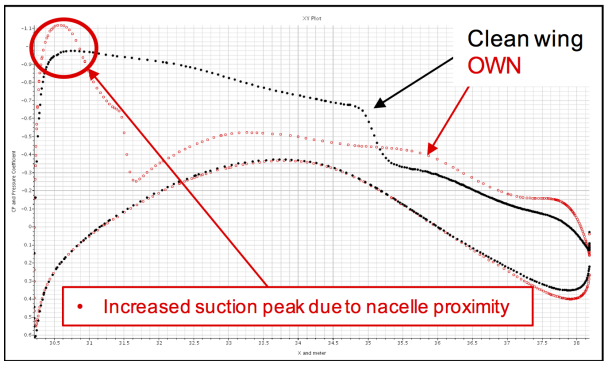

(d) Leading edge baseline Cp-distribution

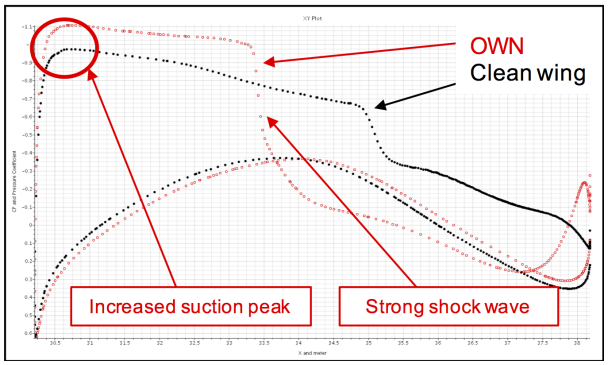

(e) Trailing edge baseline Cp-distribution

Figure 5.3: Mach contours and Cp-distribution at nacelle span location

Effect of Power Code on ΔC_D

Results show that installation drag decreases as the engine power setting increases. This is because the engine ingests more air as power code goes up, which results in less "spillage" flow to interact with. However, this effect is not as prominent as the others; the p-value is only 0.520 compared to 0.0182 for the next highest. Hence, installation drag is weakly dependent on propulsion in comparison.

Interaction of ΔX and configuration type on ΔC_D

An interaction occurs when the setting of one factor changes the effect of another. For example, Fig. 5.4 shows that ΔC_D varies almost linearly with ΔX when the configuration is of LE type, but nonlinearly when it is of TE type. For LE configuration, the former suggests that installation drag is best reduced by placing the nacelle as far away as possible from the wing, whereas the latter suggests a point of diminishing return for TE configurations. This could imply the presence of a local optimum caused by some beneficial aerodynamic interaction when the inlet nacelle is close to the trailing edge. Although additional optimization would be needed to find out for certain, this trend supports the findings of others [3, 4].

Interaction of ΔY and configuration type on ΔC_D

At LE locations, installation drag decreases as the nacelle moves outboard as shown in Fig. 5.7b, but at TE locations it's the opposite as shown in Fig. 5.7a. This interaction is an unfortunate consequence of how the coordinate system was defined, as illustrated in Fig. 5.5. For LE configurations, the gap between the nacelle and the wing increases as the nacelle moves outboard due to leading-edge sweep, whereas for TE configurations it increases inboard. Therefore, the interaction between configuration type and ΔY is most likely just the manifestation of different effect: ΔX.

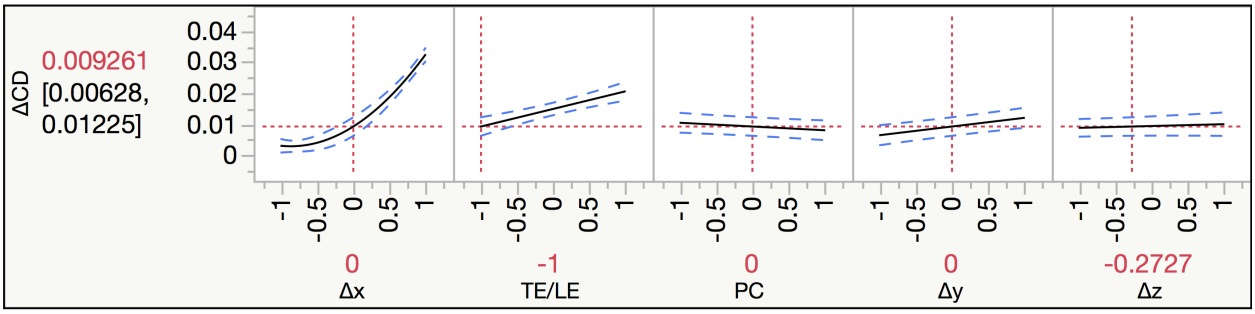

(a) Visualization of local profiles for TE configuration type

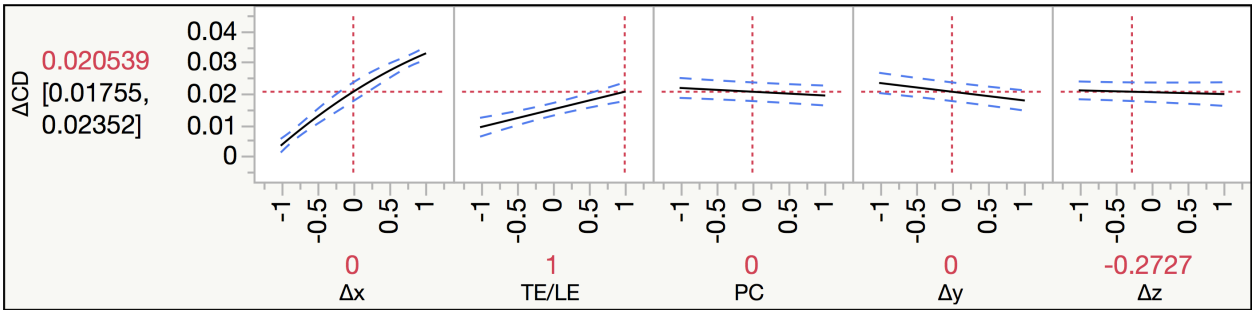

(b) Visualization of local profiles for LE configuration type

Figure 5.4: Local sensitivities analysis for ΔC_D response. *Each plot shows the local profile of the response along the dimension indicated. They correspond to the trace of the intersection between the response surface and the planes of a cartesian coordinate system whose origin lies at a point denoted by the dotted hairlines.*

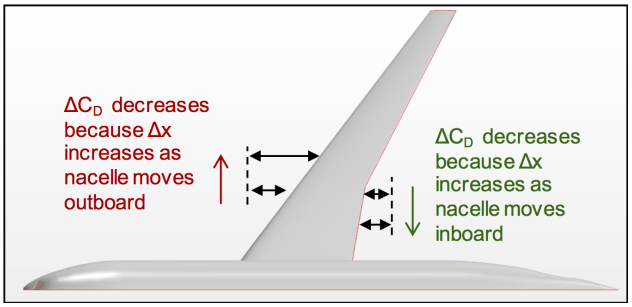

Figure 5.5: Interaction of "ΔY" and "config type" explained

Interaction of ΔZ and configuration type on ΔC_D

At LE configurations, results suggests that installation drag decreases as the nacelle moves up and away from the wing; but at TE configurations, it's the opposite as shown in Fig. 5.4. However, in both cases the variation of ΔC_D with respect to ΔZ is within the noise of the regression model. Therefore, even though the interaction itself is statistically significant (change in sign), the factor it interacts with has negligible effect on the response and so it can be neglected too.

5.3.2 Engine Pressure Recovery

The sensitivity analysis results for "change in pressure recovery" (ΔPR) are shown in Fig. 5.2b. It can be seen that the dominating effects are configuration type (TE/LE), height above the wing ΔZ, and ΔX which has a strong nonlinear influence on the response. In addition, there exist statistically significant interactions between configuration type, ΔZ, and ΔX. Each one will now be explained in more detail.

Effect of configuration type on ΔPR

Fig. 5.2b shows that pressure recovery decreases (*i.e.* ΔPR is non-zero) when the nacelle is placed at TE locations. This is because the flow entering the nacelle is non-isentropic at those locations; *i.e.* there is a strong shock on the wing ahead of the inlet, as shown Fig. 5.3b. This implies a strong dependence of propulsive efficiency on airframe aerodynamics and, as a result, there is a tradeoff between *good* installation drag and *poor* pressure recovery at TE locations. This is significant because a 2% loss in pressure recovery translates into a 9% loss in fuel burn for a representative civil transport, as shown in Fig. 5.6.

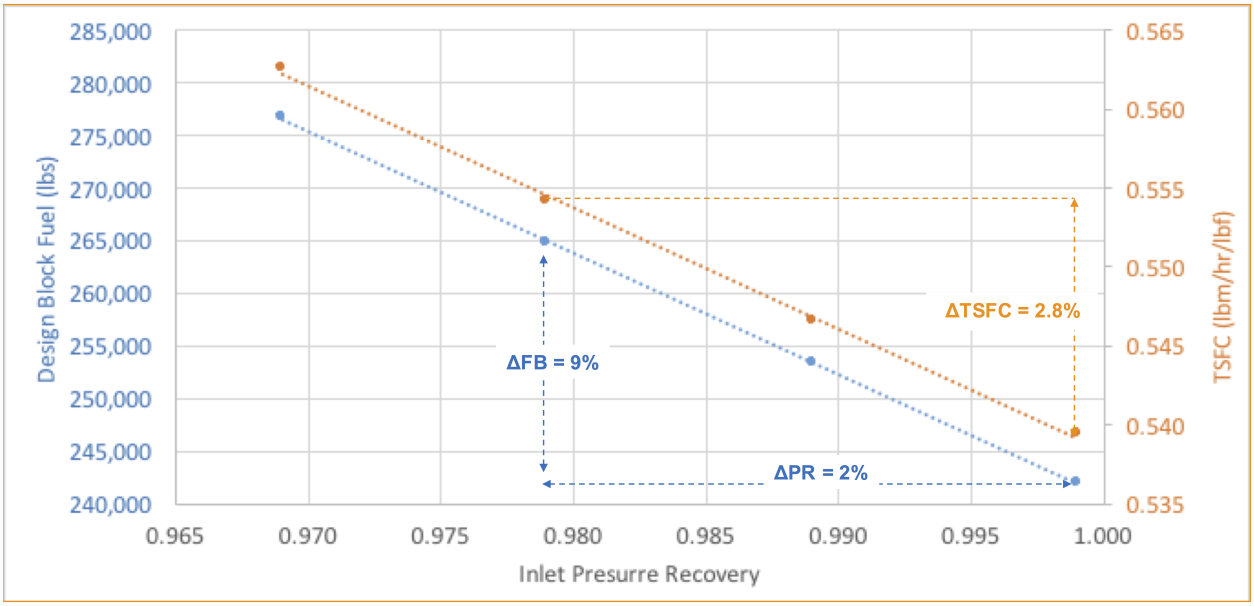

Figure 5.6: Fuel burn as a function of pressure recovery for a notional 300 passenger class transport and high bypass 94,000 lbs thrust class turbofans (generated using EDS [18])

Effect of ΔZ and configuration type on ΔPR

Fig. 5.2b shows that pressure recovery decreases as the engine moves closer to the wing; but this trend only occurs at TE nacelle locations, as shown in Fig. 5.7. Again, this implies a strong dependence of propulsion efficiency on airframe aerodynamics for TE configurations only. The trend itself makes intuitive sense, since moving the engine away from wing reduces interference and, therefore, pressure recovery losses.

Effect of ΔX and configuration type on ΔPR

Fig. 5.7 shows that pressure recovery is a nonlinear function of ΔX; but only at TE nacelle locations. This nonlinearity can be explained by taking a look at Fig. 5.8, which shows the Mach contours for three different TE configurations: $-\Delta X$, baseline, and $+\Delta X$. It can be seen ΔPR is largest for the TE baseline, which coincides with the case where the primary shock on the wing (ahead of the inlet) is strongest. Although this study did not conduct any shape optimization, this result suggests that pressure recovery will be particularly sensitive to how well the wing design is able to weaken the shock. Again, this is evidence of strong dependence between propulsive efficiency and aerodynamic design.

5.3.3 Lift Curve

The sensitivity analysis results of the lift curve parameters are shown in Figs. 5.2c and 5.2d. It can be seen that the dominating effects are configuration type (TE/LE) and ΔX, which will now be discussed in detail.

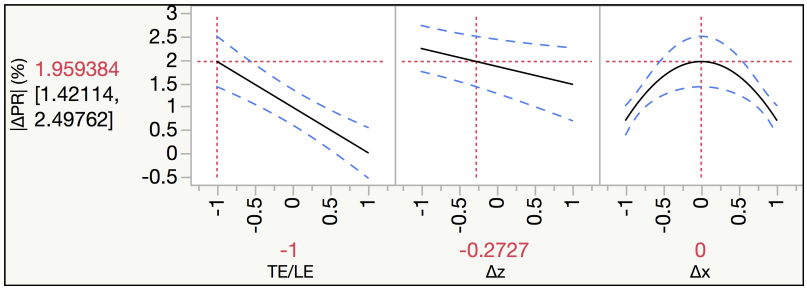

(a) Visualization of local profiles for TE configuration type

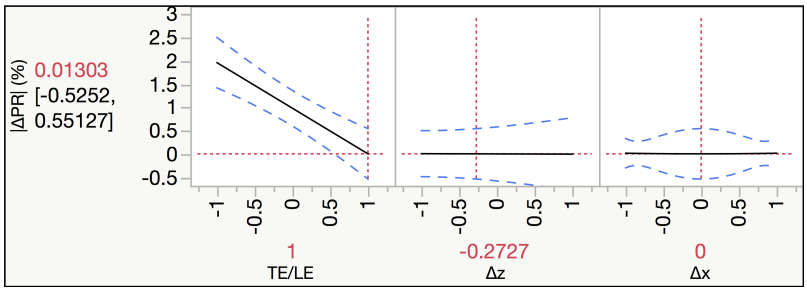

(b) Visualization of local profiles for LE configuration type

Figure 5.7: Local sensitivities analysis for ΔPR response

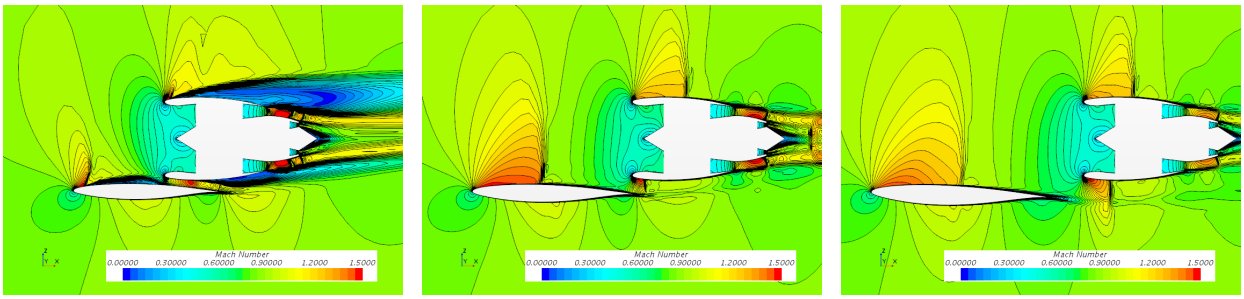

(a) Treatment 10: $\Delta PR = -0.39\%$ (b) TE Baseline: $\Delta PR = -2.5\%$ (c) Treatment 8: $\Delta PR = -0.38\%$

Figure 5.8: Mach contours at nacelle span location

Effect of configuration type on ΔC_{L_α} and ΔC_{L_0}

To better interpret the sensitivity analysis of Figs. 5.2c and 5.2d, consider Fig. 5.9 which shows how the lift curve changes for TE/LE configurations compared to the clean wing. For LE configurations, the lift curve intercept (C_{L_0}) increases and the lift curve slope (C_{L_α}) decreases, which is expected due to the Coandă effect. As the jet exhaust blows over the surface of the wing, it enhances the circulation which contributes to lift. Sensitivity with respect to angle of attack therefore decreases because circulation is now partly dependent on the engine, not just the wing. For TE configuration, C_{L_0} drops significantly because the presence of the engine creates back pressure on the wing, which effectively dumps lift.

Effect of ΔX on ΔC_{L_α} and ΔC_{L_0}

For LE configurations, there is a powered lift benefit due to the jet blowing over the wing, but this benefit erodes quickly if the nacelle moves towards the wing (*i.e.* positive ΔX), as shown in Fig. 5.10a. In fact, the convexity of the profile suggests that there is a maximum. Hence, in general, the nacelle must be close but not close to take advantage of powered lift when the configuration is of LE type. However, for TE configurations, the trend and curvature of the profiles are reversed: moving away from the wing is generally

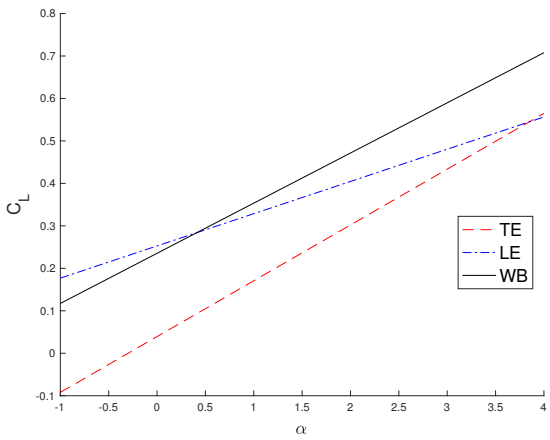

Figure 5.9: Change in lift due to configuration type

better for preserving the lift properties of the clean wing.

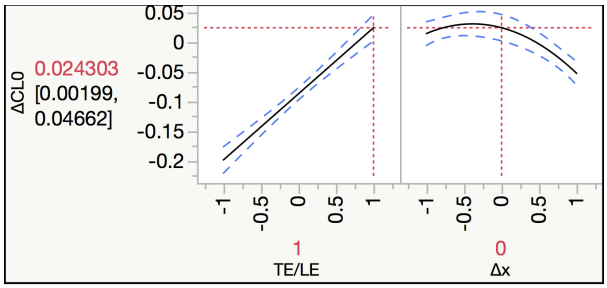

(a) Intercept *vs.* ΔX when config type = LE

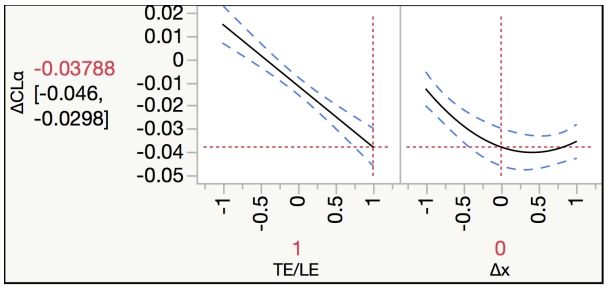

(b) Slope *vs.* ΔX when config type = LE

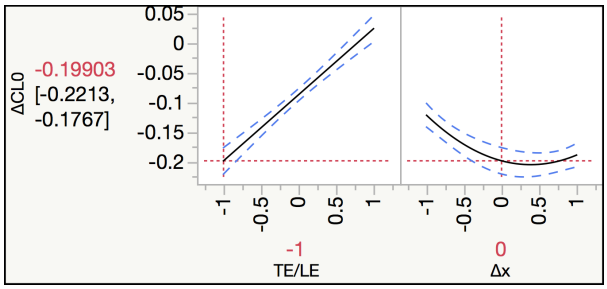

(c) Intercept *vs.* ΔX when config type = TE

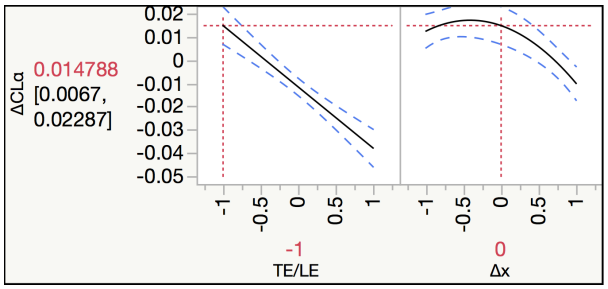

(d) Slope *vs.* ΔX when config type = TE

Figure 5.10: Local sensitivity analysis of lift curve parameters

5.4 Synthesis

This study conducted a sensitivity analysis of installation drag, pressure recovery, and lift curve parameters for podded OWN concepts with respect to the following design variables: XYZ nacelle location, configuration type (TE or LE), and engine power setting. A summary of the most significant variables per response is provided in Table 5.3. It was found that the aerodynamic and propulsion disciplines are weakly coupled: engine pressure recovery is strongly affected by airframe aerodynamics when the nacelle is placed at the trailing edge and, in return, installation drag is weakly affected by the engine's power setting, especially at TE configurations. OWN therefore represents a weakly coupled, multi-disciplinary system which requires a

coupled MDA modeling and simulation approach, as illustrated in Fig. **??**. Furthermore, it was observed that there is a tradeoff between installation drag and pressure recovery for TE configurations: the *best* nacelle location for installation drag was also found to be the *worst* for pressure recovery. Aerodynamic benefits should thus be carefully traded with propulsion penalties in order to assess the fuel burn potential of OWN concepts. Finally, this study was limited by the use of a fixed outer mold line. Future work should consider re-optimizing the nacelle for each DOE case. The authors expect that overall trends would remain, but that the relative sensitivity of ΔC_D due to ΔX would decrease, while that of due to power setting would increase.

Table 5.3: Summary of significant OWN variables

Description	C_{L_α}	C_{L_0}	C_D	PR
Config Type	✓	✓	✓	✓
ΔX	✓	✓	✓	✓
ΔZ				✓
Power Code			✓	

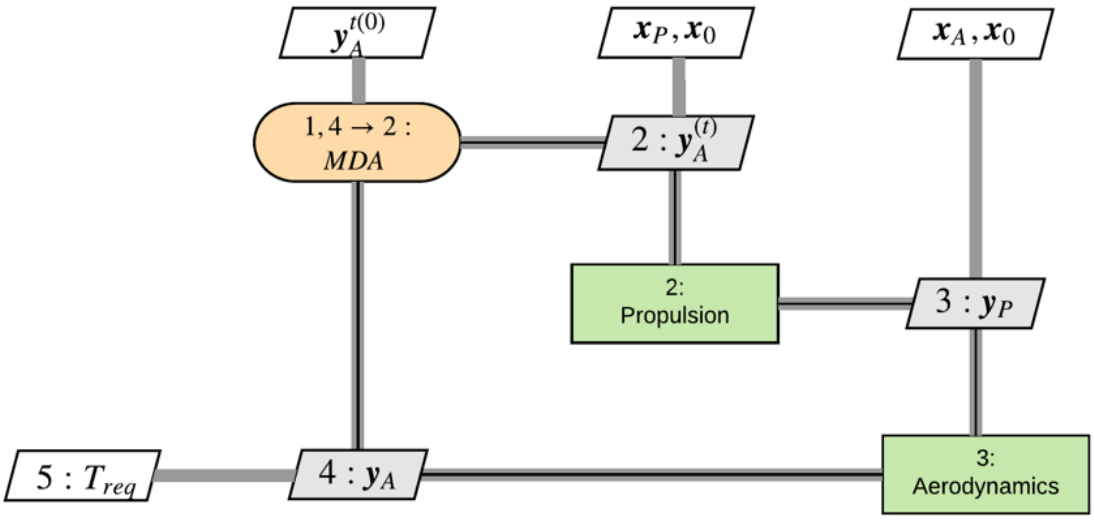

x_0 = shared variables = M, h (flight condition)

y_P = propulsion coupling variables = engine boundary conditions = $\begin{pmatrix} T_2 \\ P_2 \\ Tt_8 \\ Pt_8 \\ Tt_{18} \\ Pt_{18} \end{pmatrix}$

T_{req} = thrust required (i.e. drag)

y_A = aerodynamic coupling variables = $\begin{pmatrix} \eta_{PR} \\ T_{req} \end{pmatrix}$

x_P = propulsion variables (cycle variables)

x_A = aero variables (outer mold line)

Figure 5.11: Multi-Disciplinary Analysis (MDA) needed to capture aero-propulsive coupling

Chapter 6

Study 3: Single-Point Optimization

The purpose of this study is to minimize drag subject to fixed lift at cruise under rigid-body assumptions and ignoring trim drag. Concretely, it seeks to answer the question: is it possible to re-design the outer mold line such that the aerodynamic performance of OWN be made on par or better than the UWN baseline? This is accomplished by using optimal design methods and comparing the results before and after optimization to those of the UWN baseline.

6.1 Optimization Problem

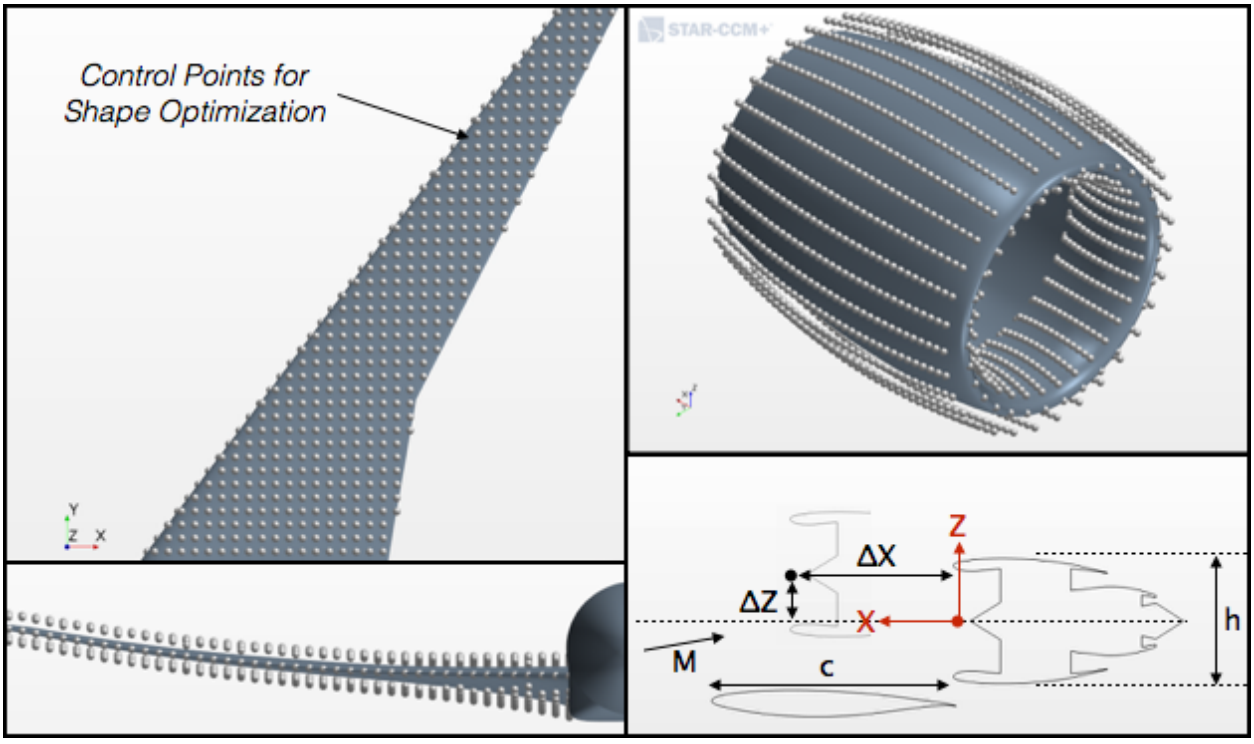

Figure 6.1: Parameterization of the design space (in this study Δx and Δz were held fixed)

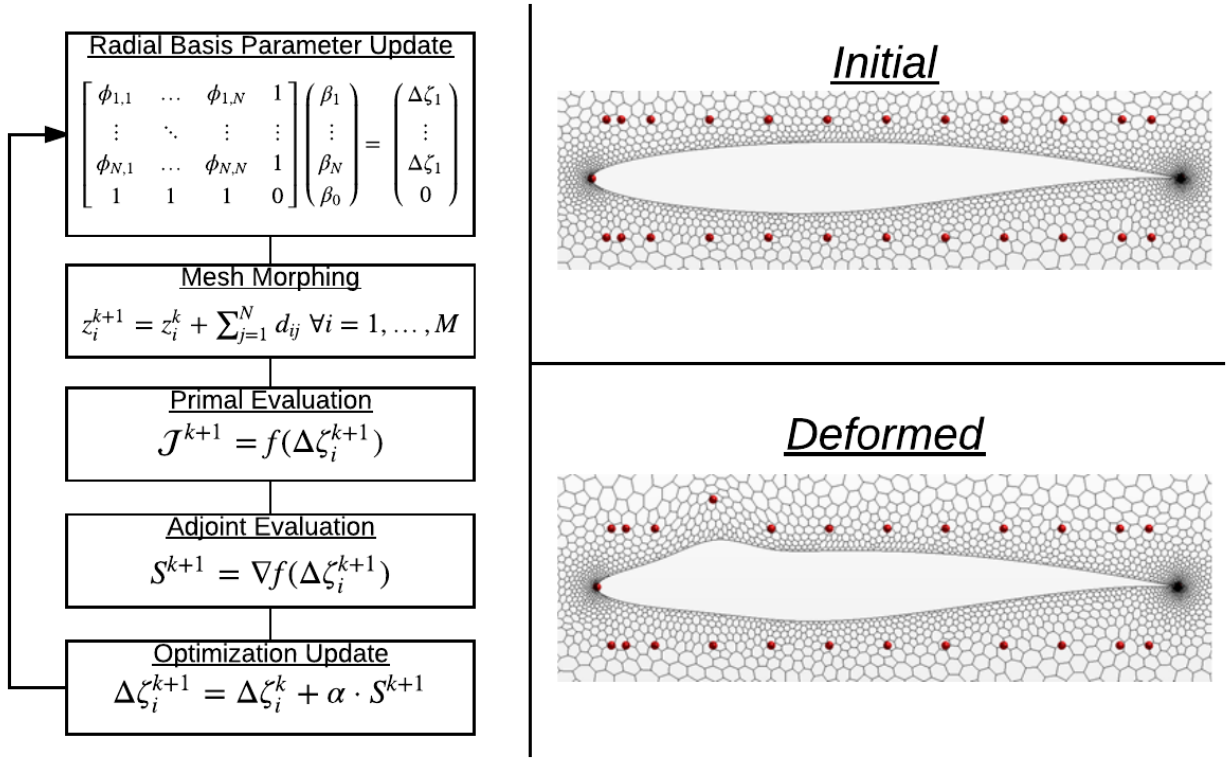

Figure 6.2: Illustration of OML morphing process. *The radial basis parameters are found by solving a linear system of equations using the known control-point positions as the training data. The mesh is then deformed using radial basis interpolation, CFD is evaluated on the deformed mesh, and the result is provided to a gradient-based optimizer which updates the design variables for the next iteration. In this figure, M is the number of grid points, N is the number of control points, α is the learning rate, and S^k is the search direction.*

Mathematically, given a fixed nacelle location, the optimization problem can be expressed as:

$$\begin{aligned} \text{Find:} \quad & \boldsymbol{z}^* = \arg\min_{\boldsymbol{z}} \Delta C_D(\boldsymbol{z}) \\ \text{subject to:} \quad & C_L = C_{L,target} \\ & \boldsymbol{z}_L \leq \boldsymbol{z} \leq \boldsymbol{z} \end{aligned} \tag{6.1}$$

where $\boldsymbol{z}^*$ denotes a vector containing the z-coordinate of N control points used for aerodynamic shape optimization of the OML, shown in Fig. 6.1 (for the nacelle, both z and y were allowed to vary). In STAR-CCM+, mesh deformation is implemented using a radial basis network as follows. For the sake of explanation, assume only the z coordinate is being varied and let Δz_j^k denote the displacement of the j^{th} control point relative to its initial position z_j^0:

$$\Delta z_j^k = z_j^k - z_j^0 \tag{6.2}$$

where k is the current optimizer iteration number. The value of Δz_j is always known since it is determined by the optimizer. However, the corresponding amount by which to deform the mesh is not; it must be determined through interpolation. The equation for a radial basis network is given by:

$$f(z) = \beta_0 + \sum_{j=1}^{N} \beta_j \phi_j(z) \quad \text{where} \quad \phi_j = ||z - z_j|| \tag{6.3}$$

where z denotes the Cartesian coordinate of any grid point in the mesh and z_j denotes that of a control point as before. The coefficients β are found by solving the following linear system:

$$\begin{bmatrix} \phi_{1,1} & \dots & \phi_{1,N} & 1 \\ \vdots & \ddots & \vdots & 1 \\ \phi_{N,1} & \dots & \phi_{N,N} & 1 \\ 1 & \dots & 1 & 0 \end{bmatrix} \begin{pmatrix} \beta_1 \\ \vdots \\ \beta_N \\ \beta_0 \end{pmatrix} = \begin{pmatrix} \Delta z_1^k \\ \vdots \\ \Delta z_N^k \\ \beta_0 \end{pmatrix} \tag{6.4}$$

where the following constraint was added:

$$\sum_{j=1}^{N} \beta_j = 0 \tag{6.5}$$

The entire optimization process is summarized notionally in Fig. 6.2.

6.2 Thrust-Drag Bookkeeping

In order to avoid double counting, it is necessary to define how thrust and drag are computed. For podded engine configurations, it is customary to delineate the two according to the engine stream-tube boundaries, as shown in Fig. 6.3.

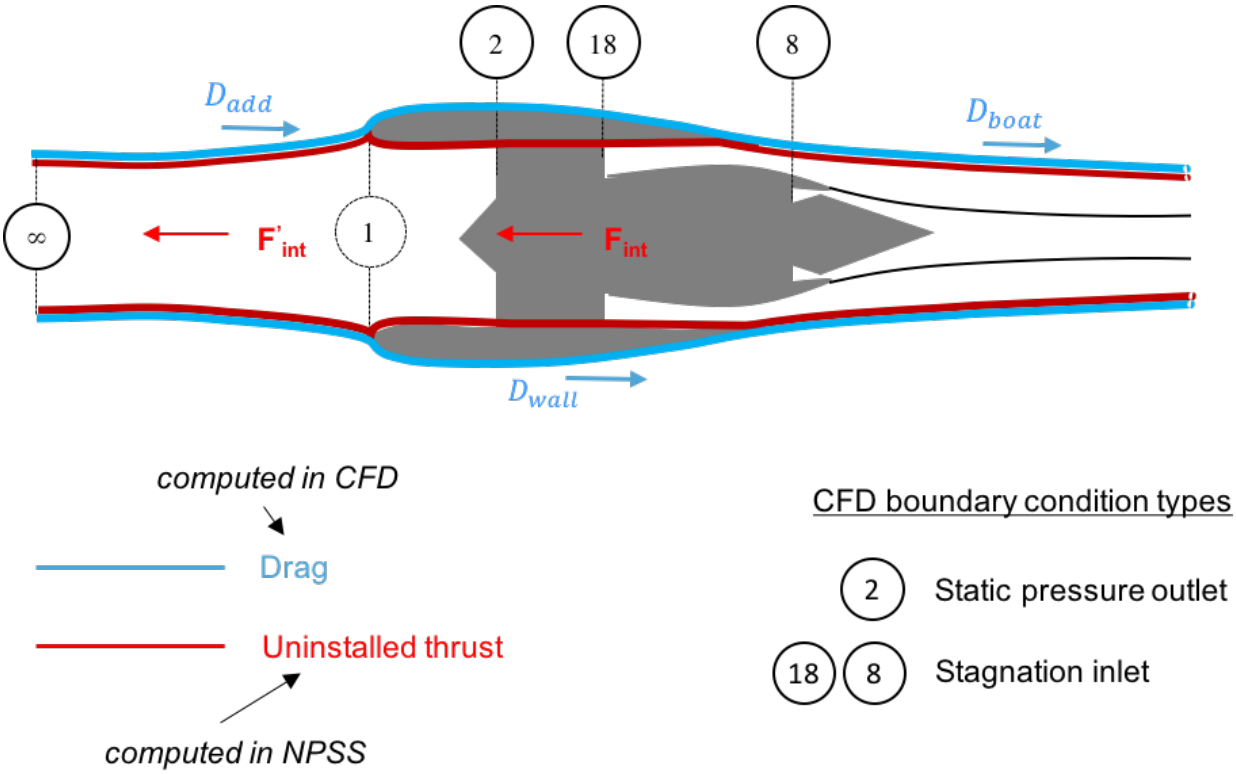

Figure 6.3: Thrust-Drag bookkeeping

Everything inside the stream tube is counted towards engine thrust; everything outside is considered airframe drag. Under this bookkeeping scheme, drag is the summation of three terms:

$$D = D_{\text{add}} + D_{\text{wall}} + \underbrace{D_{\text{boat}}}_{\approx 0} \tag{6.6}$$

The third term stands for boat-tail drag and is negligible for turbofan engines. The second term is obtained by integrating pressure and shear stress along the "external" walls of the airframe (including nacelle, wing,

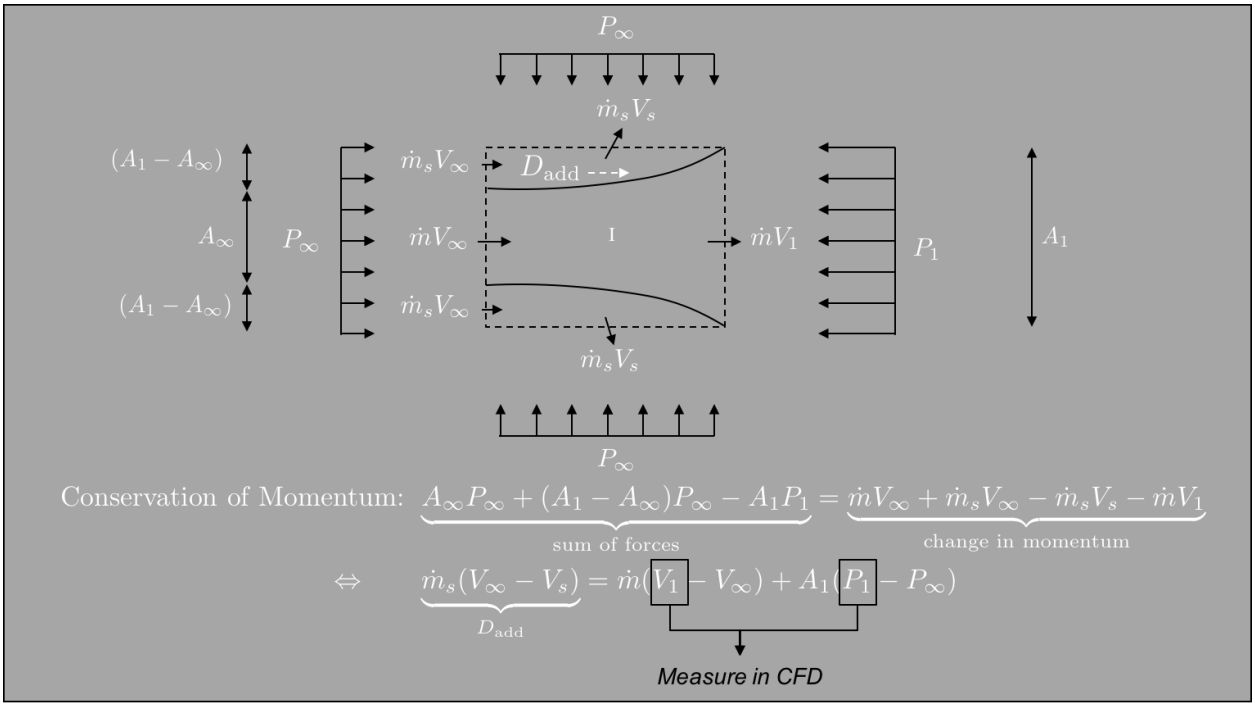

Figure 6.4: Additive drag derivation

fuselage, and empennage). The first term, however, is less intuitive. It stands for additive drag (also known as spillage drag) and arises whenever the engine requires less flow than what the inlet was designed to deliver. As a result, excess air is diverted off to the sides, spilling over the nacelle lip. The diverted flow exerts a force against the external walls of the stream tube, which must be overcome by the engine. This force is the additive drag and can be calculated from conservation of momentum applied to the control volume shown in Fig. 6.4:

$$D_{\text{spill}} = \dot{m}(V_1 - V_\infty) + A_1(P_1 - P_\infty) \tag{6.7}$$

For an OWN configuration, the properties at station 1 could be affected by the flow field of the wing (*e.g.* standing shock wave); hence, they ought to be measured in CFD. This was easily accomplished in STAR-CCM+ using mass flow averaged reports at station 1. All flow properties needed to simulate the engine's thermodynamic boundary conditions in CFD were obtained from NPSS, an industry standard cycle analysis code developed by NASA.

6.3 Results

Using Sequential Quadratic Programming (SQP), the optimizer converged in 18 iterations and the results are shown in Figs. 6.5 and 6.6 before and after optimization. It can be seen from Fig. 6.5 that the secondary shock wave was completely eliminated, while the primary shock was significantly weakened. This yields a significant drag reduction in the vicinity of optimum, as shown by the drag polars in Fig. 6.6. However, Fig. 6.7 reveals that the primary shock wave was not weakened enough: the flow entering the engine sustains a significant loss in inlet pressure recovery, defined as the total pressure ratio with the free stream.

$$\eta_{PR} = \frac{P_t}{P_{t_\infty}} \tag{6.8}$$

These results imply two things. First, they show that reshaping the OML to account for the presence of the nacelle goes a long way in improving the aerodynamic performance of OWN concepts. In this case, aerodynamic performance was on par with the UWN baseline; however, other authors have successfully

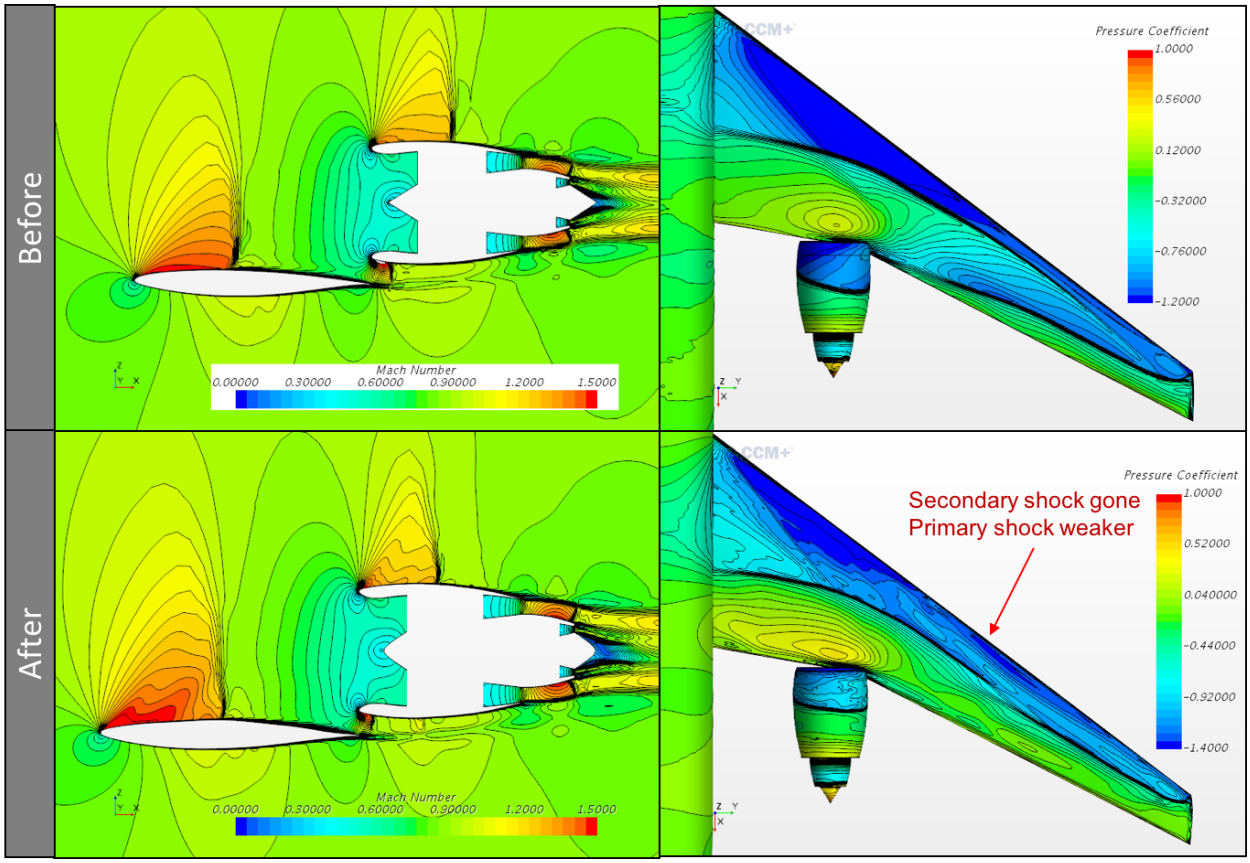

Figure 6.5: Mach and pressure contours before and after optimization

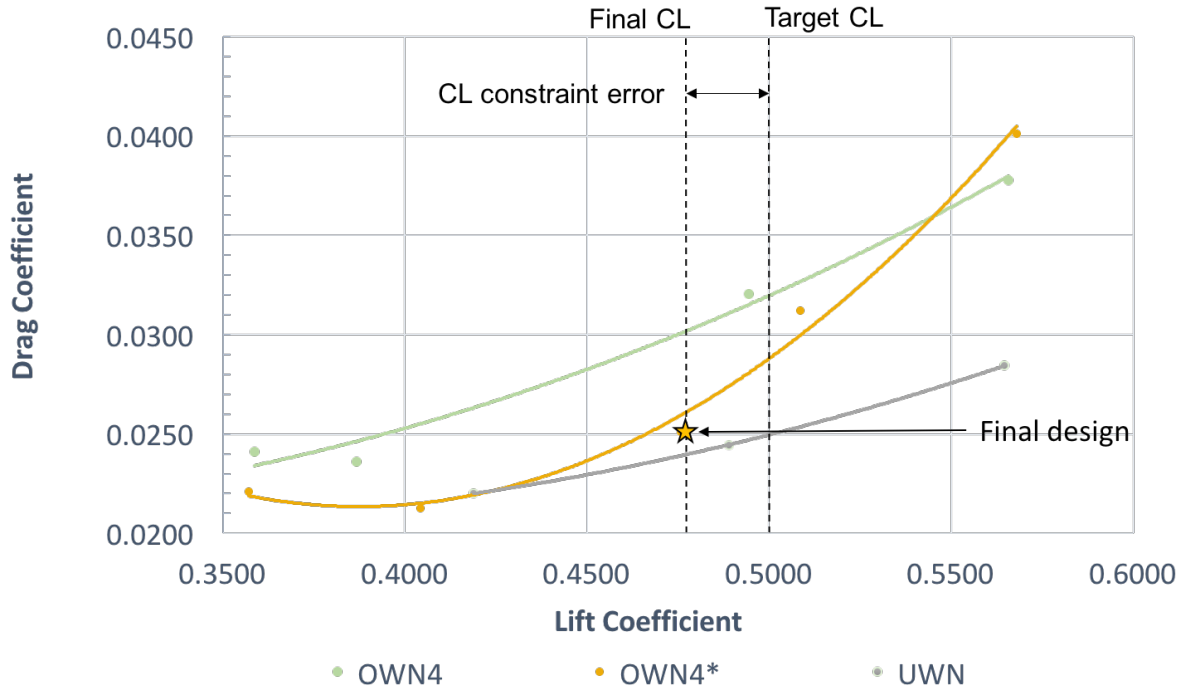

Figure 6.6: Drag polars before (OWN4) and after (OWN4*) optimization compared to UWN baseline

outperformed UWN [4, 5]. Hence, with a little effort, OWN seems to be a viable concept on the basis of aerodynamics.

Second, these results also underscore the strong influence of aerodynamic on propulsion for trailing edge OWN configuration. Specifically, should the wing experience shock waves due to unforeseen flight conditions or suboptimal design, engine efficiency will be the first to suffer. For perspective, a loss of inlet recovery of 2% (as was measured for this design) would roughly translate into a 9% fuel burn penalty for the assumed engine-airframe combination used in this study. Hence, any gains associated with improved Specific Fuel Consumption (SCF) due to favorable engine installation for high-bypass turbofans (which cannot fit under the wing), would be canceled out.

The latter does not preclude competitive OWN concepts from coming to fruition, but it does highlight an important design challenge that is not present for conventional engine installations, where the flow into the engine is decoupled from the influence of the airframe. A simple solution would be move the nacelle upward, away from the influence of the shock wave. In fact, careful examination of existing OWN concepts such as the Lockheed HWB or Honda Jet in Fig. 6.8 reveals that successful engine installations tend to be located near the trailing edge, high above the wing on a long pylon, most likely for this reason.

Figure 6.7: Pressure recovery contour plot for final design

Figure 6.8: Pylon heights for existing OWN concepts compared to current study

6.4 Synthesis

In summary, this chapter presented aerodynamic shape optimization results for a trailing edge OWN concept at a single design point, taken to be cruise. The resulting aerodynamic performance was found to be on par with the UWN baseline (although not better). Simply reshaping the OML therefore has the potential

to improve aerodynamics enough to perhaps take advantage of benefits in other disciplines such as: engine noise shielding (due to the wing acting as a shield) or improved specific fuel consumption (due to favorable engine installation for high-bypass turbofans which cannot fit under the wing). A systems analysis study would be needed to find out. However, results also revealed an important design challenge that does not exist for conventional engine installations. Namely, if the shock on the wing is not completely eliminated, the flow into the engine deteriorates and inlet pressure recovery suffers, counter-acting any improvement in propulsive efficiency. While the present authors were not able to eliminate it using adjoint methods in STAR-CCM+, leading airframe manufacturers such as Lockheed-Martin [4, 5] were very successful in doing so using inverse design methods. Hence, the quality of the final design is more a reflection on the quality of the design process than the merit of the concept itself. In particular the adjoint solver in STAR-CCM+ version 12.02 was difficult to converge compared to the primal solver, which likely resulted in slight gradient inaccuracies in the vicinity of the optimum. In addition, the radial basis parameterization yields skewed cells as the mesh deforms, which could've further contributed to gradient error. Nevertheless, results were deemed encouraging and corroborate the notion that that competitive OWN designs are achievable with a lot of effort.

Chapter 7

Conclusions

7.1 Main Findings

Engine bypass ratio (BPR) has grown significantly over the years, due to a desire for increased efficiency, and the large fan diameters that have resulted are forcing the engines so close to the wing that there is no room left for them to grow any larger due to ground clearance constraints. As BPR increases even further in the future, conventional Under-Wing Nacelle (UWN) installations will therefore no longer be possible without drastic modification of the wing and landing gear. Over-Wing nacelle concepts solve this problem by offering a convenient installation for high BPR turbofans and, additionally, offer the potential to mitigate community noise through engine noise shielding using the wing as a shield. However, OWN has historically warranted concern about unacceptably high drag levels at transonic speeds and the purpose of this research was to determine whether or not drag can be improved enough to take advantage of the aforementioned cross-disciplinary benefits. To do so, three studies were conducted with the following findings:

- Study 1 conducted a simple nacelle sweep: a fixed nacelle was translated from leading edge to trailing edge, holding all other parameters fixed. Its findings suggest that OWN LE and TE positions are more favorable than "middle" positions and exhibit comparable drag values. The flow field analysis further revealed that placing the nacelle over the wing results in greater flow acceleration between the nacelle and the wing, which can lead to a second shock and flow separation for some locations. OWN LE positions are characterized by a larger suction peak on the wing leading edge, a weaker shock wave, and the appearance of a secondary shock. OWN TE positions are characterized by a strong shock wave caused by higher back pressure due to the presence of the nacelle, and a secondary shock on the outboard wing. However, there is a beneficial suction peak on the nacelle lip and wing LE that somewhat counteract the additional wave drag penalty caused by the nacelle. At the outcome of Study 1, common sense suggested that only LE and TE positions warranted further investigation; the flow field associated with "middle" engine locations was just too poor to expect any significant improvement upon optimization.

- Study 2 conducted a sensitivity analysis of installation drag, pressure recovery, and lift curve parameters for podded OWN concepts with respect to the following design variables: XYZ nacelle location, configuration type (TE or LE), and engine power setting. The most significant variables for lift and drag were chord-wise engine placement and engine power setting. Inlet pressure recovery was significantly affected by chord-wise and vertical engine placement; however, this sensitivity was only observed at trailing edge nacelle locations due to the shock ahead of the engine on the wing. Overall, in the absence of optimization, the study found that TE nacelle placements offer an inherent drag benefit compared to leading edge placement and, therefore, became the focus for study 3. Finally, it was also found that the aerodynamic and propulsion disciplines are weakly coupled at trailing edge nacelle locations: engine pressure recovery is strongly affected by airframe aerodynamics and, in return, installation drag is weakly affected by the engine's power setting. In the future, multi-disciplinary analysis is therefore recommended to better capture the physics of such concepts.

- Study 3 conducted aerodynamic shape optimization for a trailing edge OWN concept at a single design point, taken to be cruise. The resulting aerodynamic performance was found to be on par with the UWN baseline (although not better), implying that it is possible to improve aerodynamics enough to perhaps take advantage of benefits in other disciplines. However, results also revealed that if the shock on the wing is not completely eliminated, the flow into the engine deteriorates and inlet pressure recovery suffers. Since this would counter-act any improvement in propulsive efficiency due to favorable engine installation for high-bypass turbofans (which cannot fit under the wing), special care must be taken to account for this interdependency when assessing a given OWN concept on the basis of fuel burn. Overall, results imply that a good aerodynamic shape optimization process is critical to enable competitive OWN concepts and, in addition, the engine should be mounted high above the wing on long pylons in order to minimize the influence of any shock wave on the flow entering the inlet.

7.2 Recommendations

Overall, it is the authors' opinion that either leading-edge or trailing-edge mounted OWN configurations are concepts worth investigating further, with preference on the latter. However, the feasible design space is believed to be small and, therefore, finding it heavily depends on aerodynamic shape optimization. In addition, for trailing-edge configuration, it will be critical to eliminate any shock ahead of the engine on the wing in order to ensure clean flow into the inlet, which can be accomplished through both shape optimization and placing the nacelle high above the wing, away from the influence of any shock wave. Finally, multiple design flight conditions ought to be considered in order to minimize sensitivity to changing free stream conditions across the flight envelope and, in addition, trim drag should be considered since longitudinal moment changes as the nacelle is repositioned above the wing. Aero-elasticity is also important, but the additional complexity of such an analysis is probably not worth addressing until a good OWN design can be found under rigid body assumptions.

Acknowledgments

The authors would like to thank David Hills from Airbus for not only sponsoring this project, but also offering valuable feedback along the way. The team is also grateful to the Airbus counterparts in Europe, specifically Alan Mann, Lars Joergensen, Andreas Westenberger, and Daniel Reckzeh who were kind enough to attend periodic teleconferences and offer feedback.

Bibliography

[1] Berry, D. L., "The boeing 777 engine/aircraft integration aerodynamic design process," *International Council on Aeronautical Sciences*, 1994.

[2] Berton, J. J., "Noise Reduction Potential of Large, Over-the-Wing Mounted, Advanced Turbofan Engines," Tech. Rep. April, Technical Memorandum 2000-210025, NASA, 2000.

[3] Fujino, M. and Kawamura, Y., "Wave-Drag Characteristics of an Over-the-Wing Nacelle Business-Jet Configuration," *41st Aerospace Sciences Meeting and Exhibit*, , No. January, 2003, pp. 1–11.

[4] Hooker, J. R., Wick, A., Zeune, C. H., and Agelastos, A., "Over Wing Nacelle Installations for Improved Energy Efficiency," *31st AIAA Applied Aerodynamics Conference*, 2013.

[5] Hooker, J. R., "Design of a Hybrid Wing Body for Fuel Efficient Air Mobility Operations at Transonic Flight Conditions," *52nd Aerospace Sciences Meeting*, No. January, 2014.

[6] Vassberg, J., Dehaan, M., Rivers, M., and Wahls, R., "Development of a Common Research Model for Applied CFD Validation Studies," *26th AIAA Applied Aerodynamics Conference*, , No. August, 2008, pp. 1–22.

[7] Putnam, L. E., "Exploratory Investigation at Mach Numbers from 0.40 to 0.95 of the Effects of Jets Blown over a Wing," *Nasa Tn D-7367*, , No. November, 1973.

[8] Reubush, D. E., "Effect of Over-the-Wing Nacelles on Wing-Body Aerodynamics," *Journal of Aircraft*, Vol. 16, No. 6, 1979, pp. 359–365.

[9] Henderson, W. P. and J. C. Patterson, J., "Propulsion Installation Characteristics for Turbofan Transports," *AIAA paper 83-0087*, 1983.

[10] Szodruch, J. and Kotschote, J., "On the aerodynamics of over-the-wing nacelles supported on 'stub-wings'," *21st Aerospace Sciences Meeting*, 1983, pp. 0–8.

[11] Wimpress, J. K. and Newberry, C. F., *The YC-14 STOL Prototype: Its Design, Development, and Flight Test An Engineer's Personal View of an Airplane Development*, AIAA, 1998.

[12] Norton, B., *Stol Progenitors: The Technology Path to a Large STOL Transport and the C-17A*, AIAA, 2002.

[13] Kathen, H., "VFW 614, quiet short haul airliner," *Archive Set 114*, 1963.

[14] Birckelbaw, L. D., "High speed aerodynamics of upper surface blowing aircraft configurations," *AIAA paper 92-2611*, 1992.

[15] Yamato, H., Okada, N., and Bando, T., "Flight Test Of The Japanese USB STOL Experimental Aircraft ASKA," *AIAA paper 1988-2180-116*, 1988.

[16] Hall, G. W., "Flight Research At NASA AMES: A Test Pilot's Perspective," Technical Memorandum 100025, NASA, 1987.

[17] Taylor, N., Gammon, M., and Vassberg, J., "The NASA Common Research Model: a Geometry Handling Perspective," *46th AIAA Fluid Dynamics Conference*, 2016.

[18] Kirby, M. and Mavris, D., "The Environmental Design Space," *26th International Congress of the Aeronautical Sciences*, Anchorage, Alaska, 14 - 19 September 2008.

[19] Periaux, J., Bugeda, G., Giannakoglou, K., and Mantel, B., *Optimum Aerodynamic Design and Parallel Navier-Stokes Computations ECARP ??? European Computational Aerodynamics Research Project*, Vol. 61 of *Notes on Numerical Fluid Mechanics*, Vieweg, Weisbaden, 1998.

[20] Gray, J. S., Mader, C. A., Kenway, G. K., and Martins, J., "Approach to Modeling Boundary Layer Ingestion using a Fully Coupled Propulsion-RANS Model," *58th AIAA/ASCE/AHS/ASC Structures, Structural Dynamics, and Materials Conference*, AIAA SciTech Forum, American Institute of Aeronautics and Astronautics, jan 2017.

[21] Hines, W. W., Montgomery, D. C., Goldsman, D. M., and Borror, C. M., *Probability and Statistics in Engineering*, Wiley, 2003.

[22] Myer, R. and Montgomery, D., *Response Surface Methodology: Process and Product Optimization Using Designed Experiments*, Wiley, 2002.

[23] Raymond H. Myers, Douglas C. Montgomery, and Anderson-Cook, C. M., *Response Surface Methodology*, Wiley, John Wiley & Sons Inc., New York, 2nd ed., 2009.

[24] Plackett, R. L. and Burman, J. P., "The Design of Optimum Multifactorial Experiments," *Biometrika*, Vol. 33, No. 4, 1946, pp. 305.

[25] Berguin, S. H., *A method for reducing dimensionality in large design problems with computationally expensive analyses*, Ph.D. thesis, Georgia Institute of Technology, 2015, pp. 16 – 37.